Influence of fracture scale heterogeneity on the flow properties of three-dimensional discrete fracture networks (DFN)

Jean-Raynald de Dreuzy, Yves Méheust, Géraldine Pichot

Influence of fracture scale heterogeneity on the flow properties of three-dimensional discrete fracture networks (DFN)

J.-R. de Dreuzy,[1,2] Y. Méheust,[2] and G. Pichot[3]

Received 18 May 2012; revised 28 August 2012; accepted 10 September 2012; published 16 November 2012.

[1] While permeability scaling of fractured media has been so far studied independently at the fracture- and network- scales, we propose a numerical analysis of the combined effect of fracture-scale heterogeneities and the network-scale topology. The analysis is based on $2{\cdot}10^6$ discrete fracture network (DFNs) simulations performed with highly robust numerical methods. Fracture local apertures are distributed according to a truncated Gaussian law, and exhibit self-affine spatial correlations up to a cutoff scale L_c. Network structures range widely over sparse and dense systems of short, long or widely distributed fracture sizes and display a large variety of fracture interconnections, flow bottlenecks and dead-ends. At the fracture scale, accounting for aperture heterogeneities leads to a reduction of the equivalent fracture transmissivity of up to a factor of 6 as compared to the parallel plate of identical mean aperture. At the network scale, a significant coupling is observed in most cases between flow heterogeneities at the fracture and at the network scale. The upscaling from the fracture to the network scale modifies the impact of fracture roughness on the measured permeability. This change can be quantified by the measure α_2, which is analogous to the more classical power-averaging exponent used with heterogeneous porous media, and whose magnitude results from the competition of two effects: (i) the permeability is enhanced by the highly transmissive zones within the fractures that can bridge fracture intersections within a fracture plane; (ii) it is reduced by the closed and low transmissive areas that break up connectivity and flow paths.

Citation: de Dreuzy, J.-R., Y. Méheust, and G. Pichot (2012), Influence of fracture scale heterogeneity on the flow properties of three-dimensional discrete fracture networks (DFN), *J. Geophys. Res.*, *117*, B11207, doi:10.1029/2012JB009461.

1. Introduction

[2] Natural fractured media display a strong hydraulic complexity coming from the fractures' internal topography, from their arrangement in complex networks, and from the interaction of the fractures with the environing rock matrix [*Bear et al.*, 1993; *National Research Council*, 1996]. As a result, flows are generally localized in complex structures and the bulk hydraulic properties display a large variability both inside a given medium and between different media. [*Clauser*, 1992; *Hsieh*, 1998; *Tsang and Neretnieks*, 1998]. Only few of these flow structures can be identified deterministically by geophysical and hydraulic methods [*Rubin and Hubbard*, 2006; *Yeh and Liu*, 2000]; most of them can only be modeled statistically. Such an approximated statistical representation is sufficient for a large range of purposes. For example the knowledge of the detailed flow structure is not crucial to estimate an effective permeability. With this in mind, a prerequisite of modeling consists in determining which fracture properties are essential for hydraulic and transport properties. This has been the original goal of the Discrete Fracture Network approach (DFN). DFNs mimic natural fractured media by representing each fracture individually. They have first been designed toward homogenizing fractured media [*Long et al.*, 1982], and further applied to understanding the flow structures of complex fracture networks [*Davy et al.*, 2006a; *de Dreuzy et al.*, 2001b, 2001c, 2002, 2004a; *Le Goc et al.*, 2010; *Leung and Zimmerman*, 2010], permeability and dispersivity upscaling [*Baghbanan and Jing*, 2007; *Charlaix et al.*, 1987; *de Dreuzy et al.*, 2001a, 2010; *Frampton and Cvetkovic*, 2007, 2009; *Mettier et al.*, 2006; *Park et al.*, 2001; *Snow*, 1969] and, more generally, the definition of the right modeling approach [*Cello et al.*, 2009; *Davy et al.*, 2006a; *Ji et al.*, 2011; *Jourde et al.*, 2007; *Long and Witherspoon*, 1985; *Painter and Cvetkovic*, 2005; *Sahimi*, 1993]. As a further interest, DFNs can extract key information on flow properties from the large geological and geophysical data available on fracture media [*Bonnet et al.*, 2001; *Davy et al.*, 2010]. In this sense

[1]Institute of Environmental Analysis and Water Studies, CSIC, Barcelona, Spain.
[2]Géosciences Rennes, UMR CNRS 6118, Université de Rennes 1, Rennes, France.
[3]IRISA, INRIA, Université de Rennes 1, Rennes, France.

Corresponding author: J.-R. de Dreuzy, Géosciences Rennes, UMR CNRS 6118, Université de Rennes 1, Campus de Beaulieu, FR-35042 Rennes CEDEX, France. (jean-raynald.de-dreuzy@univ-rennes1.fr)

0148-0227/12/2012JB009461

the DFN approach is used to "precondition" equivalent continuum heterogeneous approaches, to which it becomes complementary rather than competitive [*Hsieh*, 1998; *Neuman*, 2005]. It is according to this logic that the generalized radial flow model has been developed [*Barker*, 1988], used [*Cappa et al.*, 2006; *Le Borgne et al.*, 2004], justified [*de Dreuzy and Davy*, 2007; *de Dreuzy et al.*, 2004b] and extended [*Acuna and Yortsos*, 1995; *Cello et al.*, 2009].

[3] So far, hydraulic DFN studies have been performed mostly in 2D. The three-dimensional (3D) flow simulation models have been developed essentially either as a proof of concept [*Dershowitz and Fidelibus*, 1999; *Lenti and Fidelibus*, 2003; *Long et al.*, 1985; *Maryka et al.*, 2004] or for specific site studies [*Cacas et al.*, 1990a, 1990b; *Kalbacher et al.*, 2007]. The only existing 3D stochastic DFN simulations have demonstrated first the broad range of transport transit times within a given fracture networks, as well as between average travel times measured from different simulation runs [*Nordqvist et al.*, 1996], and second the possibility of removing smaller fractures from fracture networks dominated by the longest fractures [*Wellman et al.*, 2009]. 3D stochastic DFN modeling has been hindered because of the difficulty of generating meshes of good quality with classical mesh generation algorithms [*Kalbacher et al.*, 2007; *Maryka et al.*, 2004; *Vohralik et al.*, 2007]. Flow simulations in complex 3D fracture networks require either modifications of the geometrical configurations that are detrimental to the mesh generation on the whole 3D structure [*Erhel et al.*, 2009a], or the decoupling of the mesh generation between fractures using Mortar-like methods [*Pichot et al.*, 2010].

[4] In the fracture network models mentioned above, the basic geometric and hydraulic object is the single fracture. Its hydraulic behavior is classically described by a scalar transmissivity: independently of the flow conditions, the ratio of the overall volumetric flow through the fracture to the norm of the corresponding pressure gradient (computed between the fracture's inlet and outlet) is equal to the ratio of the transmissivity to the fluid's absolute viscosity, the transmissivity being solely dependent on the fracture geometry. The first approximation model for a fracture is the parallel plate, for which the transmissivity is proportional to the plate separation distance to the power of 3 (see, among many others, *Zimmerman and Bodvarsson* [1996b]). In reality, the distribution of local apertures within a geological fracture is nonuniform, due to the roughness of the two facing rock walls. Early experiments [*Cook*, 1992; *Durham and Bonner*, 1995; *Durham*, 1997; *Witherspoon et al.*, 1979] demonstrated that the resulting transmissivity is different from that of a parallel plate model of identical mean aperture [*Cook*, 1992; *Durham and Bonner*, 1995; *Durham*, 1997; *Witherspoon et al.*, 1979]. Numerical modeling of the flow has shown how the deviation from the parallel plate model increases with fracture closure and how it results from aperture heterogeneities-induced flow channeling within the fracture plane. Indeed, the rough walls of a rock joint exhibit peculiar statistical properties: their topographies are scale-invariant over a broad range of length scales [*Brown and Scholz*, 1985; *Power and Durham*, 1997; *Schmittbuhl et al.*, 1993] and are matched over a characteristic "correlation" scale [*Brown et al.*, 1986; *Isakov et al.*, 2001], so that the aperture distribution is also scale invariant from at least the scale of the rock grain up to the latter correlation length [*Brown et al.*, 1986; *Glover et al.*, 1998]. This scale invariance is controlled in first approximation by a scalar parameter usually denoted Hurst exponent; over a broad range of length scales and material types (including geological fracture walls), rough surfaces resulting from brittle fracturing have been measured to exhibit a Hurst exponent very close to 0.8 [*Bouchaud et al.*, 1990]. The spatially correlated fluctuations of the aperture field allow for the existence of correlated large aperture "channels" and low aperture "barriers" within the aperture plane; numerical simulations based on the Reynolds equation [*Brown*, 1987] have shown that these channels and barriers are responsible for a channeling of the flow [*Brown*, 1987], which impacts the permeability of a given fracture, for a given direction of the macroscopic flow. That permeability may also be estimated through a generalized critical path analysis from a critical barrier defined as the smallest permeability line orthogonal to flow [*Talon et al.*, 2010a, 2010b]. Numerical simulations show that, depending on how the channels and barriers are oriented with respect to the macroscropic flow, they can either ease the flow through the fracture and make it more permeable than a parallel plate model of identical mean aperture [*Méheust and Schmittbuhl*, 2000], or hinder the flow with respect to that through a parallel plate model [*Brown*, 1987; *Méheust and Schmittbuhl*, 2000, 2001]. However, if one considers a population of statistically identical fractures, favorable configurations are less frequent than unfavorable ones, so that the mean behavior corresponds to a transmissivity lower than that of the parallel plate of identical mean aperture [*Méheust and Schmittbuhl*, 2001]. In addition, the variability over the statistics increases with the fracture closure, defined as the ratio of the aperture spatial variability to its mean value. Another puzzling finding by *Méheust and Schmittbuhl* [2001] is that a given rough fracture does not have an intrinsic transmissivity: it depends in particular on the flow orientation with respect to the fracture at least at scales smaller than the correlation length. The role played by the correlation length has however been little studied. *Méheust and Schmittbuhl* [2003] have shown that as soon as the correlation length is significantly smaller than the distance between the inlet and outlet, the fracture behaves as a parallel plate. Note also that the average behavior of a statistically homogeneous population of fractures depends only weakly on the spatial correlations [*Méheust and Schmittbuhl*, 2001]: it is mostly identical to that of a population of uncorrelated fractures.

[5] Up to now little has been tempted to model the hydraulic effects of the fracture-scale aperture heterogeneity and of the network-scale intricate structure simultaneously. A first intuitive approximation would consist in replacing the internally heterogeneous fractures by parallel plates having the same equivalent transmissivity T or equivalently a distance between the plates equal to $(12T)^{1/3}$. It is however both practically difficult and theoretically questionable. First, as explained above, a rough fracture does not have an intrinsic permeability independent of the boundary conditions, which makes this approximation both wrong from a theoretical point of view and arbitrary from a practical point of view. Second, the organization of flow potentially exploits the 2D aperture heterogeneity within the fracture plane and 3D high transmissivity shortcuts at the network scale simultaneously: the inlets and outlets for flow in a fracture are intersections with other fractures, and therefore depend on the network structure. In the most dramatic configurations, local fracture

closure may lead to the disconnection of some hydraulic paths and consequently induce an extended flow reorganization at the network scale.

[6] Such effects can only be addressed using a three-dimensional model that accounts both for (i) interior fracture geometrical heterogeneities and (ii) the fracture arrangements in networks of complex topology. Due to previous technical limitations of 3D simulation methods, the flow localization effects at the fracture- and at the network- scale have so far been analyzed separately, with the exception of one article [*Hamzehpour et al.*, 2009] that presented a model based on very restrictive assumptions. First, the fractures had a binary aperture distribution, that is, the apertures within a fracture plane could be either null or have a nonzero value given once for all, for all open regions in all fractures in the DFN. Second, all fractures had the same size. Third, the fracture density was much larger than that corresponding to the percolation threshold. In what follows, thanks to recently developed 3D simulation methods [*Erhel et al.*, 2009a], we analyze the combined effects of fracture-scale heterogeneity and network-scale structure on the permeability of the bulk fractured media, investigating DFNs in which individual fractures (i) have a realistic aperture distribution that is self-affine up to the correlation length in open regions of the fracture plane, and (ii) have sizes that can be as large as the medium size L and as small as $L/10$. We investigate different types of network structures, including networks with a power law size distribution of the fracture sizes, and vary the fracture density from configurations far above the percolation threshold, for which mean field approximations are likely to be relevant, down to the vicinity of the percolation threshold, for which only extensive Monte-Carlo numerical experiments can give insight into the systems' hydraulic behavior.

[7] In what follows, we describe the studied model at the fracture and network scales successively, as well as the flow models (section 2) and their numerical implementation (section 3). Because of a lack of reference results at the fracture scale for the range of closures considered, we first study the mean fracture-scale permeability (section 4), which we then use when discussing the network scale equivalent permeability (section 5). We finally discuss the hydraulic interaction between the network topology and the fracture scale heterogeneity, in section 6.

2. Discrete Fracture Network Model

[8] Among the large range of possible Discrete Fracture Network models (DFNs), we have chosen a classical design and added complexities at the fracture scale. The rock matrix is assumed to be almost impervious in comparison to the fractures so that flow only occurs inside fractures. At the fracture scale, the flow complexity consists in a channeling that arises from the self-affine aperture distribution of the individual fracture. At the network scale, the flow complexity arises from the fracture size distribution and depends on the density of the fractures in the network. Other assumptions have been taken as simple and standard as possible. The originality of this study lies in that the stochastic DFN flow simulations are performed with a resolution high enough for the flow complexity to be solved inside the smallest fractures.

[9] We successively present the network structure, the geometrical characteristics both of a single fracture and of the ensemble of fractures, and the flow models at the fracture and network scales.

2.1. Fracture Network Structure

[10] For the sake of simplicity, fractures are modeled as disks. The fracture size thus corresponds to the diameter of the disk. No location or position is favored, meaning that the fracture orientation and position distributions are uniform within the system. Under these simplifications, the two geometrical features that control hydraulic properties at the network scale are the uniform scalar density of fractures and the fracture size-distribution. In fact, both these features have a dramatic impact on the connection and homogenization scales of the medium. The connection scale is the scale above which networks become connected on average. The homogenization scale is characteristic of flow channeling; it is defined as the characteristic distance between two adjacent flow channels carrying equally large flow rates [*de Dreuzy et al.*, 2001b].

[11] Let us first discuss the size distribution. Observations of geological fractured media have shown that the density function for their fracture size is broad-ranged and exhibits no characteristic length scale; it is well modeled by a power law in the form:

$$f(L_f) = \frac{a_{3D} - 1}{L_{fmin}^{-a_{3D}+1}} L_f^{-a_{3D}} \text{ for } L_f \in \left[L_{fmin}; L_{fmax}\right] \quad (1)$$

where $-a_{3D}$ is the characteristic exponent for the probability density, and $[L_{fmin}; L_{fmax}]$ is the range of modeled fracture sizes [*Bonnet et al.*, 2001; *Davy et al.*, 2010; *Segall and Pollard*, 1983]. The exponent a_{3D} controls the relative proportion of longer and shorter fractures. Field data, in particular from outcrops, provide essentially the 2D exponent a_{2D}, which ranges between 1 and 3.5 [*Bonnet et al.*, 2001]. For uncorrelated fractures, the 3D and 2D exponents are related according to $a_{3D} = a_{2D} + 1$ [*Darcel et al.*, 2003b; *Piggot*, 1997]; the exponent a_{3D} thus ranges in the interval [2; 4.5].

[12] While the observed fracture size distribution extends over several orders of magnitude, 3D flow simulations cannot account for such a scale dynamics and remain technically limited to a narrower scale interval, covering around one order of magnitude. Because of this limitation, three types of size distribution are considered in what follows. In the first type, fractures are all much longer than the system size (Figure 1, left). This type of 3D system has been widely used since the pioneering work of *Snow* [1969]. From the hydraulic point of view it corresponds to a power law distribution with $a_{3D} = 2$ [*Bour and Davy*, 1998] because in power law distributed systems with $a_{3D} = 2$ all fractures that contribute to flow extend across the whole medium. In the second type, all fractures have the same size L_{fmin} significantly smaller than the system size L (Figure 1, middle). This case corresponds to the classical percolation theory scheme [*Stauffer and Aharony*, 1992] and is obtained when a_{3D} goes to infinity (Figure 1, left). In the third type, fracture sizes effectively follow a power law distribution with an exponent $a_{3D} = 3.5$ on a scale range extending from L_{fmin} to the system size L (Figure 1, right). As the impact of a given fracture on percolation is rated by the cube of its size because of excluded volume arguments [*Balberg et al.*, 1984; *de Dreuzy et al.*, 2000], both smaller and longer fractures effectively contribute to network connectivity for $a_{3D} = 3.5$ [*Bour and*

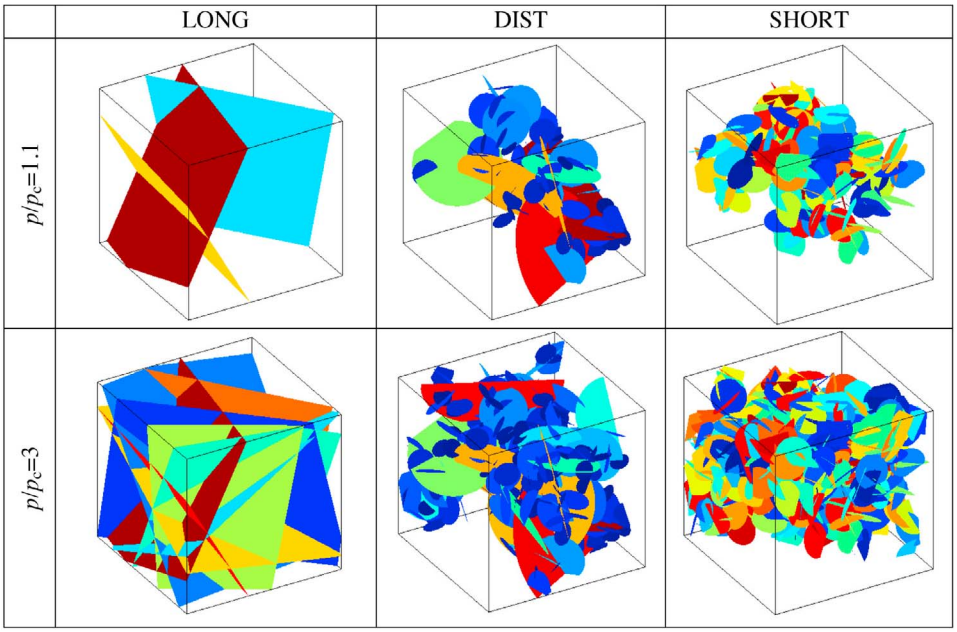

Figure 1. Examples of discrete fracture networks: (left) with long fractures (LONG) and L/L_{fmin} = 10, (middle) with a power law fracture size distribution (DIST) and L/L_{fmin} = 10, and (right) with uniform fracture sizes and L/L_{fmin} = 5 (SHORT). (top) Two networks that are close to the percolation threshold (p/p_c = 1.1) and (bottom) those that are significantly above it (p/p_c = 3). Note that colors do not have any further meaning than identifying the different fractures.

Davy, 1998; *de Dreuzy et al.*, 2000]. We shall denote those three types of network as SHORT, LONG and DIST (Table 1), respectively.

[13] As mentioned above, the other key characteristic parameter of the fracture network is the fracture density. We consider the two extreme cases of sparse and dense fracture networks. Below the percolation threshold, hydraulic properties are determined neither by the network structure nor by the fracture internal characteristics but rather by rock matrix properties [*Hsieh et al.*, 1993]. The sparsest networks of interest in our framework are thus networks at the percolation threshold. We denote as dense networks those with a fracture density much larger than the threshold density. Whatever the configuration, density is always defined by reference to the percolation threshold. We choose the percolation parameter p as the measure of density; it is defined from the truncated third moment of the fracture size distribution, according to

$$p = \frac{N}{L^2} \int_{L_{fmin}}^{L_{fmax}} (\min(L_f, \alpha L))^3 \; f(L_f) dL_f \qquad (2)$$

where N is the fracture number and αL is the mean size of a fracture truncated by the boundaries of the cubic domain of linear size L [*de Dreuzy et al.*, 2000]. The percolation parameter is less classical than other measures like the fracture number per unit length P_{30} or the total fracture surface per unit volume P_{32} [*Davy et al.*, 2006b]. The advantage of the percolation parameter over other measures is that it provides the same rating of the position of the fracture network with respect to the percolation threshold whatever the fracture size distribution. In what follows, the sparse network case corresponds to $p = p_c$, while the dense network case will be taken as $p = 3p_c$ for the LONG and DIST configurations. Because of numerical limitations, the fracture density is bounded toward larger values by time constraints imposed on running the flow simulations.

2.2. Aperture Distribution of Individual Fractures

[14] As described at length in the introduction, geological fractures are defined by two facing rock surfaces, which are rough but can be approximated at large scales as two parallel planes. If the fracture walls do not touch each other, the

Table 1. Common Characteristics of the Discrete Fracture Networks[a]

Parameter	Notation	Value
	Network Scale	
Domain size	[L, L, L]	DIST: L/L_{fmin} = 10 SHORT: L/L_{fmin} = 5
Orientation distribution		Uniform
Position distribution		Poissonian
Length distribution	SHORT	$L_f = L_{fmin}$
	DIST	$L_{fmin} \le L_f \le L_{fmax}$
	LONG	$L_f = L_{fmax}$
Fracture density	p/p_c	$1.05 \le p/p_c \le 3$
	Fracture Scale	
Roughness exponent	H	0.8
Cutoff length	L_c	$0.5 \le L_c/L_{fmin} \le 3$
Fracture closure	c_{frac}	$0.5 \le c_{frac} \le 3$

[a]Density is defined by the percolation parameter p with p_c its value at percolation threshold. The maximum fracture length L_{fmax} is not equal but close to the system size L as the truncation of the largest fractures by the cubic system generates a complex object, the typical size of which may be somewhat larger than the system size L.

distribution of local apertures, a, is simply the difference between the two facing topographies, and its mean value $\bar{a}$ is equal to the separation between the two average planes, traditionally denoted mechanical aperture, a_m. When the wall topographies are brought sufficiently close to each other, they touch at one point, at which a goes to zero. In our model, we allow further closure of the fracture by "melting" the overlapping rock masses into each other. In other words we put all negative local values of the aperture to zero. The motivation for this procedure is mostly simplicity, and its mechanical validation may be considered doubtful; it is however common practice in the field [*Brown*, 1987; *Thompson and Brown*, 1991; *Thompson*, 1991]. A fracture with closed zones has a mean aperture that is larger than its mechanical aperture: $\bar{a} > a_m$.

[15] As the two fracture walls of a natural fracture exhibit Gaussian height distributions of identical amplitudes, and due to the closure rule presented above, the aperture field is distributed according to a Gaussian law truncated so that a values always be nonnegative:

$$p(a) = \begin{cases} \frac{1}{\sigma_a\sqrt{2\pi}} e^{-\frac{(a-a_m)^2}{2\sigma_a^2}} & \text{if } a \geq 0 \\ 0 & \text{if } a \leq 0 \end{cases} \quad (3)$$

where $\sigma_a = \sigma_a(L_f)$ is the standard deviation of the overall distribution prior to the truncation of negative values. Furthermore, the spatial organization of this distribution obeys the following constraints: wall topographies are (i) self-affine and (ii) matched above a characteristic scale L_c, which we denote correlation length. Note that the meaning of that correlation length is unusual, since the two surfaces are uncorrelated with each other at scales smaller than L_c, and identical above. Consequently, prior to the truncation of negative aperture values, the aperture field is self-affine up to the correlation length L_c and exhibits no spatial correlations at scales larger than L_c [*Brown*, 1995; *Méheust and Schmittbuhl*, 2003]. In other words, the standard deviation of a computed on a window of size l, $\sigma_a(l)$, and prior to its truncation to only positive values, scales as [*Schmittbuhl et al.*, 1995]:

$$\begin{cases} \sigma_a(l) \propto l^H & \text{for } 0 \leq l \leq L_c \\ \sigma_a(l) \propto L_c^H & \text{for } L_c \leq l \leq L_f \end{cases}; \quad (4)$$

where H is the Hurst exponent (or roughness exponent) that is characteristic of the self-affinity. Note that after truncation of the negative values, the effective standard deviation of a computed on a window of size l, $\sigma_a^*(l)$, is smaller than $\sigma_a(l)$.

[16] The above scale-invariance property corresponds to a power spectral density $S = |\tilde{a}|^2$ (where the $\tilde{a}$ denotes the Fourier transform of a) of the aperture field prior to truncation in the form [*Méheust and Schmittbuhl*, 2003]:

$$\begin{cases} S(\mathbf{k}) = |\tilde{a}|^2(k_c) & \text{for } k \leq k_c \\ S(\mathbf{k}) = |\tilde{a}|^2(k_c)\left(\frac{k}{k_c}\right)^{-2(1+H)} & \text{for } k \geq k_c \end{cases} \quad (5)$$

where $\mathbf{k}$ is the two-dimensional Fourier vector along the fracture plane, k is its Euclidian norm, and k_c is the wave number corresponding to the correlation length. This description in the Fourier space is completely equivalent to that in terms of spatial correlations.

[17] Provided that the Hurst exponent be set to 0.8 [*Bouchaud et al.*, 1990], our statistical model of rough fracture is based on three parameters: the ratio of the fracture length to the correlation length, L_f/L_c; the root mean square amplitude of the aperture field, which we can choose to define at the scale of the fracture, $\sigma_a = \sigma_a(L_f)$; and the mechanical aperture a_m. We introduce the *a priori fracture closure* as the ratio of σ_a to the mechanical aperture:

$$c_{frac} = \frac{\sigma_a}{a_m}. \quad (6)$$

c_{frac} represents the magnitude of the roughness relative to the distance between the two mean planes of the fracture walls. It is important to keep in mind that $\bar{a}$ and σ_a^*, differ all the more from a_m and σ_a, respectively, as c_{frac}, and therefore the proportion of closed regions within the fracture plane, are larger. Consequently, the *effective fracture closure*

$$c_{frac}^* = \frac{\sigma_a^*}{\bar{a}}$$

differs all the more from c_{frac} as the closure is larger (Figure 2a). From equation (3) it follows that

$$p(a/a_m) = \begin{cases} \frac{1}{c_{frac}\sqrt{2\pi}} e^{-\frac{(a/a_m - 1)^2}{2c_{frac}^2}} & \text{if } a \geq 0 \\ 0 & \text{if } a \leq 0 \end{cases}$$

and the proportion of closed regions within the fracture plane is simply

$$g(c_{frac}) = p(a = 0) = \frac{1}{2}\left[1 - \text{erf}\left(\frac{1}{\sqrt{2}c_{frac}}\right)\right]. \quad (7)$$

Figure 2b illustrates the dependency of g on c_{frac}. Note that the distribution of the local fracture transmissivities, $p(T)$, can be derived directly from the $p(a)$ *by* assuming locally the validity of the cubic law:

$$p(T) = \frac{1}{\sigma_a\sqrt{2\pi}} \frac{1}{3\beta^{1/3}T^{2/3}} \exp\left(-\frac{\left((T/\beta)^{1/3} - \sigma_a/c_{frac}\right)^2}{2\sigma_a^2}\right) \quad (8)$$

for $T > 0$, with $\beta = 1/12$. The aperture and transmissivity distributions are illustrated in Appendix A.

[18] In conclusion, the aperture distribution of a rough fracture is fully described by the set of parameters (c, σ_a, L_f/L_c).

2.3. Variability Among the Fractures of a Network

[19] A given DFN consists of rough fractures all described by the same statistical model. The variability within the population of fractures arises from two effects: first, the variability among the values chosen for c, σ_a, and L_f/L_c; and second, through the stochastic nature of the aperture field generation for individual fractures. We have chosen to consider a fractured medium that is homogeneous to some extent, in that the correlation length of its fractures, L_c, and the fluctuations of their roughness, if measured at the same given scale for all, are

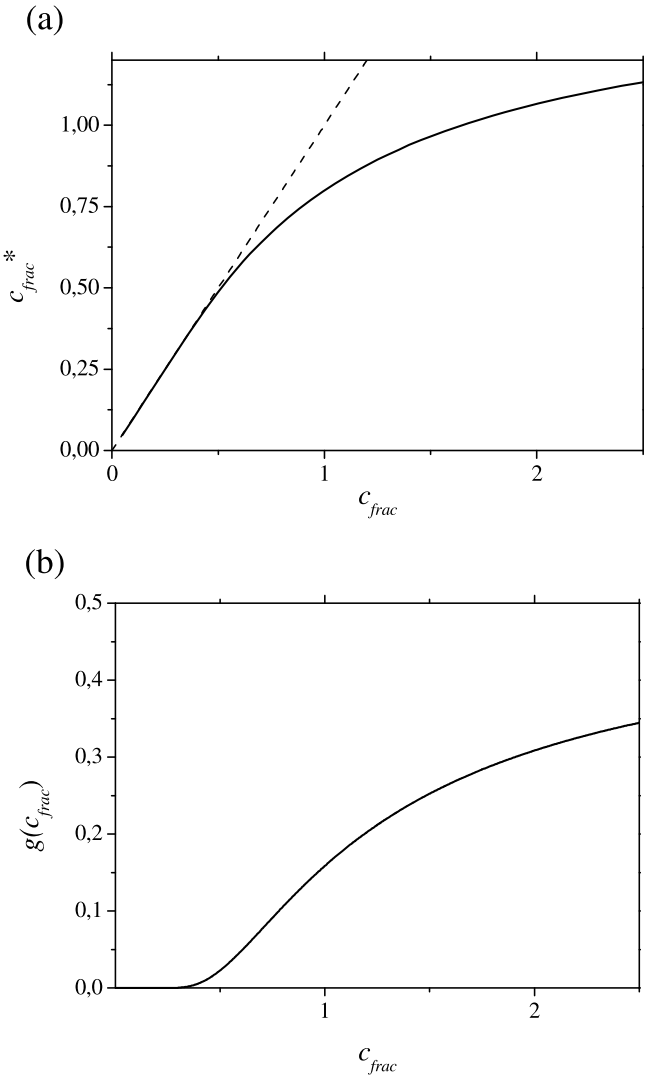

Figure 2. Evolution of (a) the effective fracture closure c^*_{frac} and (b) the proportion of closed regions of a fracture as a function of the imposed a priori fracture closure, c_{frac}.

both uniform across the medium; consequently, $\sigma_a(L_c)$ is uniform. Furthermore, we assume that the mechanical load per surface unit, F_N/L_f^2, that is imposed on each fracture plane, and which is responsible for its partial closure, is uniform across the medium as well, and independent of the fracture orientation: in other words, the stress tensor within the medium is uniform and isotropic. These are reasonable simple assumptions if all fractures in the network arise from the same fracturing process. Another more subtle assumption, which we have not addressed here, would consist in correlating the mechanical load and the fracture orientations.

[20] Let us now relate the assumption of uniform load per surface unit and the variability of the fracture closures in the DFN. *Persson* [2001] developed a theory of contact mechanics between randomly rough surfaces. If the contact is elastic, it is well known [see, e.g., *Johnson*, 1985] that the contact between two surfaces is equivalent to that between a flat plane and a rough surface corresponding to the negated aperture field. *Persson* [2001] addressed in particular the case of a rough topography that is self-affine up to a given cutoff scale. This corresponds exactly to the closure of our synthetic rough fractures, the system size being our fracture size L_f and the cutoff scale being our correlation length L_c. These theoretical results by *Persson* [2001], later verified by numerical simulations [*Persson et al.*, 2002], showed that the total contact surface is always proportional to the mechanical load (computed by considering asperities defined down to the smallest meaningful scale), that is, that closure occurs under constant stress on contact points. Furthermore, if L_c is independent of the system size L_f, the contact surface S_c is also independent of L_f, but if L_c is equal to L_f, then S_c is proportional to L_f^H. Expressed for the fractures in our DFNs, it means that the ratio of the closed area of a given fracture's plane to its total area is

$$\frac{S_c}{L_f^2} = F \cdot \frac{F_N}{L_f^2} \cdot \min\left(L_c^H, L_f^H\right) \tag{9}$$

where both the stress factor F_N/L_f^2, the cutoff scale L_c and the prefactor F are uniform over the medium. The mechanical properties of the bulk material (elastic modulus and Poisson ratio) are here hidden inside the prefactor F, which also features the geometric parameters that are characteristic of the rough surfaces: typical size of the smallest asperities, cutoff length L_c, and Hurst exponent H [*Persson*, 2001]. As the relation between the a priori closure c_{frac} of a fracture and S_c/L_f^2 is the one to one function g defined by equation (7), identical for all fractures in the medium (at least if $\sqrt{S_c} \le L_c$), one can define a global *medium closure*, c, as

$$c = g^{-1}\left(F \cdot \frac{F_N}{L_f^2} \cdot L_c^H\right) \tag{10}$$

such that each individual a priori fracture closure can be written as

$$\begin{aligned} c_{\mathrm{frac}} &= c && \text{if } L_f \ge L_c \\ c_{\mathrm{frac}} &= g^{-1}\left(g(c) \cdot \left(\frac{L_f}{L_c}\right)^H\right) && \text{if } L_f \le L_c \end{aligned} \tag{11}$$

[21] Let us examine what this means for the different types of DFNs. In SHORT systems, all fractures have the same size L_f and thus the same fracture closure. In LONG systems, all fractures have a length larger than L_c and thus a constant fracture closure c_{frac} equal to c. For DIST systems with L_c from 0.5 to 3 and $L = 10$, the a priori closure of a fracture depends on its length. For these systems we make the approximation that the a priori individual fracture closures are all equal to the medium closure c. This is not true for the majority of fractures that have length smaller than L_c, but holds for the large fractures that contribute most significantly to the overall flow.

[22] In conclusion, assuming a uniform and isotropic stress tensor within the medium results in all fractures having the same a priori closure in SHORT and LONG systems. We make the approximation that this property also holds for DIST systems. The a priori fracture closure c_{frac} is then a scalar quantity that is uniform over the whole medium: for DFNs of types LONG and DIST, it is equal to the medium closure c, while for DFNs of type SHORT, it is related to c according to equation (11). Note that in contrast to c_{frac}, the individual effective fracture closures c^*_{frac} can exhibit a

dispersion around a mean value due to the stochastic nature of the topographies. In what follows, we shall study the permeability of the medium as a function of the a priori fracture closure c_{frac}.

2.4. Flow Model in Individual Fractures

[23] The flow in fractures is modeled according to the lubrication approximation, i.e., assuming a creeping flow (no inertial effects) and a gradient of the aperture field topography much smaller than 1 [*Méheust and Schmittbuhl*, 2001; *Zimmerman and Bodvarsson*, 1996a, 1996c]. It implies that (i) the pressure field can be considered to only depend on the two-dimensional position along the mean fracture plane, and (ii) that the local flux $\boldsymbol{q}$ field, defined as the integral along the fracture aperture of the flow velocity field, is related at each point of the mean fracture plane to the local pressure gradient, $\boldsymbol{\nabla} P$, according to a local cubic law in the form:

$$\mathbf{q} = -\frac{a^3}{12\eta}\boldsymbol{\nabla} P \tag{12}$$

where a is the local aperture as defined above and η is the viscosity of water. Note that equation (12) is identical to the well-known cubic law relating the volumetric flow through a parallel plate fracture to the macroscopic gradient defined at the fracture scale. By definition [see *Johnson*, 1985] the local flux is a conservative quantity, which yields the well-known Reynolds equation:

$$\boldsymbol{\nabla}\cdot\left(a^3\boldsymbol{\nabla} P\right) = 0. \tag{13}$$

To our knowledge, this equation was first utilized to study the flow through a geological rough fracture by *Brown* [1987]. Inverting this equation provides the pressure field in the fracture plane from the knowledge of the aperture field and of the pressure conditions on the fracture domain boundaries; the local fluxes are then computed through equation (12), and the total volumetric flux Q through the fracture as the integral of local fluxes through an appropriate section of the fracture.

[24] Models based on the Reynolds equation suffer from the limitations mentioned above. However, the assumption of the slowly varying aperture field is valid at sufficiently large length scales, due to its self-affine nature: its gradient goes to 0 at very large scales, and to infinity at infinitely small scales; since it is mostly the few larger Fourier modes of the aperture field that control the transmissivity of the fracture [*Méheust and Schmittbuhl*, 2003], the limitations of the Reynolds equation are mostly those inherent to the Stokes flow approximation [*Brown et al.*, 1995; *Witherspoon et al.*, 1980]. In other words, our study is only valid for Reynolds numbers smaller than 1 in all fractures of the network. This is not a very severe limitation under hydrogeological conditions.

2.5. Flow Model at Network Scale

[25] In order to define a bounded open domain, the network is embedded into a cube of edge size L, orientated along the directions of a x, y, z coordinate system with the origin at the center of the cube. The matrix is considered impervious, thus the flow domain is the union of the N_{F} fractures Ω_{f} ($f = 1..N_{\mathrm{F}}$), with N_{I} intersection S_{k} ($k = 1..N_{\mathrm{I}}$) between the fractures. The flow model of the previous section (at the fracture scale) is complemented with continuity conditions on fracture intersections S_{k}, which are written:

$$\begin{aligned} &h_{k,f} = h_k, \forall f \in F_k \\ &\sum_{f\in F_k} \mathbf{q}_{k,f}\cdot\mathbf{n}_{k,f} = 0 \end{aligned} \tag{14}$$

where F_{k} is the set of fractures intersecting on S_{k}, h_{k} the head on the intersection S_{k}, $h_{k,f}$ the trace of the head on S_{k} in fracture f, $\mathbf{q}_{k,f}$ the flow through the intersection in the fracture f, and $\boldsymbol{n}_{k,f}$ the normal to the intersection S_{k} in the fracture Ω_{f} [*Erhel et al.*, 2009a; *Noetinger and Jarrige*, 2012; *Vohralik et al.*, 2007]. The chosen boundary conditions are classical permeameter boundary conditions: two opposite faces of the cube have fixed heads (Dirichlet type boundary conditions) and the four orthogonal faces are impervious (Neumann type boundary conditions). Boundary conditions on the fracture f are summarized as:

$$\begin{aligned} &h = h_+ \text{ on } \Gamma_f \cap \Gamma_{y+} \\ &h = h_- \text{ on } \Gamma_f \cap \Gamma_{y-} \\ &\mathbf{q}\cdot\mathbf{n} = 0 \text{ on } \Gamma_f \backslash \left(\Gamma_{y+} \cup \Gamma_{y-}\right) \end{aligned} \tag{15}$$

where Γ_{x-}, Γ_{x+}, Γ_{y-}, Γ_{y+}, Γ_{z-}, Γ_{z+} are the six faces of the cube and Γ_{f} is the border of the fracture f. The direction of the head gradient along y will be referred to as the main flow direction.

3. Numerical Methods

[26] We have developed a complete software suite, called MP_FRAC, which generates a random DFN and simulates a steady state flow in this network, with various boundary conditions [*Erhel et al.*, 2009a]. This software is integrated in the platform H2OLab [*Erhel et al.*, 2009b]. The generation methods for the networks and for the fracture-scale aperture distributions are classical and are recalled in Appendices B and C for completeness. The flow solution method for single fractures is classical but features an original measurement of the connectivity prior to the solving of the flow, while the flow solution method for full fracture networks is less classical and applied for the first time to a geophysical study. They are both described below.

3.1. Independent Resolution of the Flow Inside a Single Fracture

[27] In section 4 below, we compute the transmissivity of individual rough fractures inside a DFN and investigate the statistics of the fracture transmissivities, independently of their position in the DFN. With this procedure, we aim at measuring the typical impact of fracture wall roughness on the hydraulic behavior of a given fracture within the network. This impact will be utilized for the interpretation of the full network-scale simulation, which are described in section 3.2 and interpreted in section 5.

[28] The transmissivity of each individual rough fracture is obtained by computing the pressure field directly on the square grid on which the aperture field is generated (see section 2.2), and with simple boundary conditions: a constant pressure head in-between two of the facing boundaries (denoted inlet and outlet), and periodic boundary conditions on the two lateral boundaries. The resolution consists in the inversion of equation (13) using a conjugate gradient method

and a dual grid in order for pressure gradients to be computed in a symmetrical manner at the proper grid nodes. See *Méheust and Schmittbuhl* [2001, 2003] for a detailed description of the numerical method.

[29] For these flow simulations at the fracture scale, the connectivity of the fracture is checked prior to computing the flow, in the following manner. The aperture field is thresholded into a mask that only takes two values: 0 for closed areas of the fracture plane, 1 otherwise. The clusters corresponding to a mask value of 1 are then labeled using the Hoshen-Kopelman algorithm [*Hoshen*, 1997]; if at least one of these clusters extends throughout the fracture size, parallel to the macroscopic pressure head, there exists one connected path of nonzero apertures from the inlet to the outlet of the fracture. If not the fracture is considered non-connected, and we do not compute the flow through it. Note that in this manner we also discard a very small proportion of fractures for which the flow would be possible thanks to the periodic boundary conditions, along a direction that is very oblique with respect to that of the macroscopic pressure gradient; for these fractures, the flow (and, consequently, the transmissivity) computed using periodic lateral boundary conditions is very different from what it would be using impermeable lateral boundary conditions, which is why we choose to consider more realistic to define them as non-connected hydraulically.

[30] For connected networks, we compute the equivalent fracture permeability, K_F, using Darcy's law at the fracture scale

$$K_F = \frac{Q}{L\Delta h} \tag{16}$$

where Q is the total volumetric flow through the inlet face of the domain, Δh is the head difference between the domain inlet and outlet, and L is the characteristic fracture size. We focus on the dimensionless ratio of the fracture permeability K_F to the permeability K_0 of a parallel plate fracture with an aperture $a = \sigma_a(L_f)/c_{frac}$ identical to the mechanical aperture of the rough fracture. We recall that $\sigma_a(L_f)$ is the standard deviation of the overall distribution and c_{frac} is the medium fracture closure. Whatever the fracture size distribution, K_0 is defined unequivocally. Averages will be performed on 500 simulations of individual fractures discretized on 512 × 512 grids.

3.2. Flow Modeling and Simulation in the 3D Fracture Network

[31] The numerical model of the flow in the entire network, resolved at the fracture scale, is based on the Mixed Finite Element method, mainly for two reasons: it ensures both local and global mass conservation and it provides an accurate velocity field, which can be used in subsequent transport simulations. We implemented the so-called RT0 scheme [*Brezzi and Fortin*, 1991; *Raviart and Thomas*, 1977]. The networks considered have a very specific geometry: it is a 3D intricate structure of 2D domains. Since the matrix is impervious, the mesh is 2D inside each fracture, 1D at the intersections between fractures, and a 3D set of 2D intersecting domains at the network scale. A first difficulty is to generate this mesh, since it cannot be handled directly by a mesh generator. A second difficulty is to ensure head and flow continuity at the intersections of the fractures and a third challenge is to solve the resulting linear system.

[32] To generate the mesh, a first approach is to first discretize the boundaries and the intersections, then the 2D fractures. However, this method induces very small angles because of the intricate geometry and may fail for some networks [*Mustapha*, 2005]. Therefore, we designed a new method, introducing a pre-processing step where intersections are discretized with a regular grid. Moreover, local adjustments are necessary to guarantee geometrical properties. We developed this approach in both a conforming and a non-conforming setting [*Erhel et al.*, 2009a; *Pichot et al.*, 2010, 2012]. Local modifications and a non conforming method are also used in *Vohralik et al.* [2007]. With a hybrid method and a conforming mesh, it is finally quite easy to ensure the continuity conditions at the intersections, because of the choice of the main unknowns (the head at each edge of the mesh) [*Erhel et al.*, 2009a]. With a non-conforming mesh, we used the Mortar framework to write the discrete problem [*Pichot et al.*, 2010]. However, the pre-processing step induces particular cases where some parts of intersections are common to three fractures or more. Thus, we had to generalize the Mortar method to deal with these configurations [*Pichot et al.*, 2012]. The conforming mesh method has been validated with the non-conforming mesh method [*de Dreuzy et al.*, 2012] and is used throughout this paper.

[33] Linear equations written at each edge of the mesh express local mass conservation. The resulting linear system $Ax = b$, where x is the trace of hydraulic unknowns on edges and b accounts for boundary conditions, is large. It has as many unknowns as edges in the mesh but is sparse, with roughly five nonzero coefficients per line for a mesh with triangles [*Erhel et al.*, 2009a]. The matrix A of the system is SPD (symmetric positive definite), also for the non-conforming case. Thus several solving algorithms can be used: a direct method, based on the Cholesky factorization; an algebraic multigrid method; a preconditioned conjugate gradient method, with various preconditioners; a domain decomposition method [*Poirriez*, 2011]. High performance computing is required to handle very large systems. Once the system is solved, it is easy to compute the head inside each triangle and the transverse flux at each edge, using the RT0 scheme.

[34] An example of the resulting flows is shown in Figure 3. It addresses the sparse DIST network of Figure 1 for the two configurations of smooth (parallel plate) and rough fractures, and for a fracture closure c_{frac} of 1. The two configurations exhibit a strong channeling both at the network scale and at the fracture scale and a wide variety of flow values. Comparison between the two demonstrates the strong influence of the fracture aperture distribution on the volume occupied by the flow: it is heavily channelized within the fracture planes in the rough fracture configuration, appearing more 1D than 2D. The focus of the present article is to determine to which extent these differences in flow structures impact the equivalent permeability of the medium.

3.3. Network Connection and Equivalent Permeability

[35] Local closure of fractures may induce network disconnection at larger scales. It occurs when closed areas prevent flow through a fracture plane that the network structure would otherwise (i.e., at moderate fracture closure) direct a

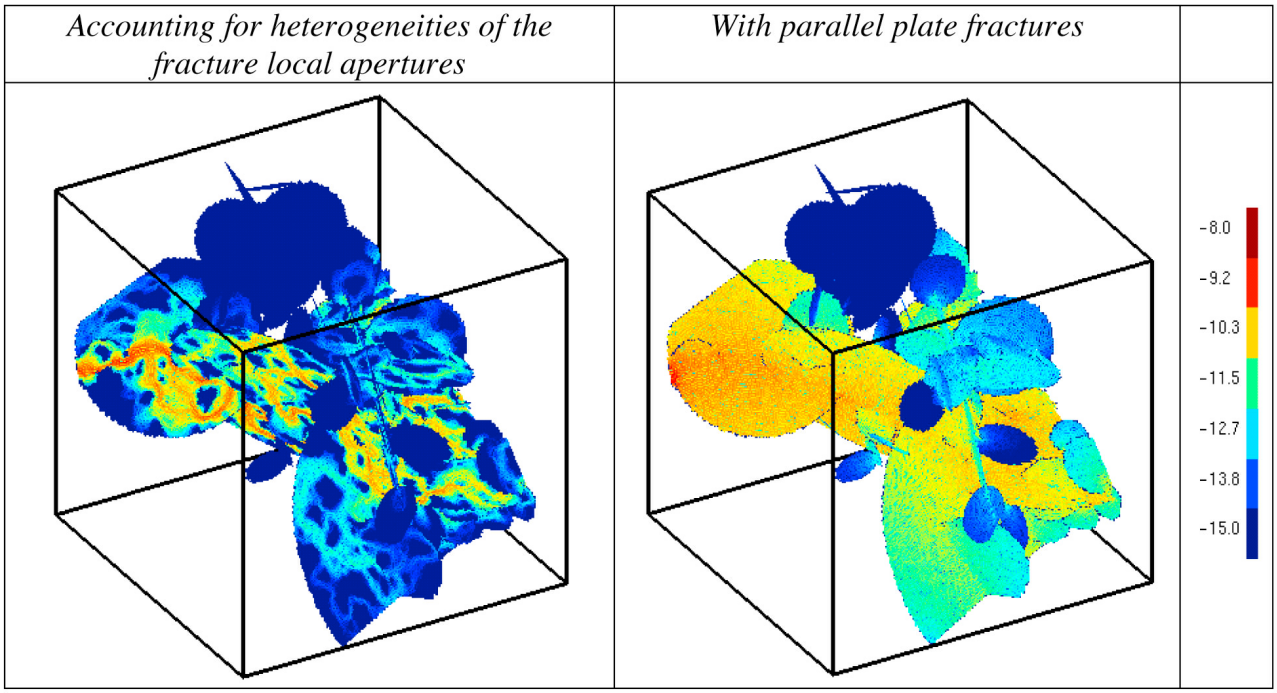

Figure 3. Flow field within the sparse DIST network shown in Figure 1 (top middle), (left) when heterogeneities of the fracture local apertures are taken into account ($c_{\mathrm{frac}} = 1$) and (right) when fractures are modeled as parallel plates. Scale on the right displays the logarithm of the mean flow value within a mesh cell.

significant volumetric flow to. A particular case occurs when an intersection between two fractures that is an essential hydraulic link at moderate fracture closures falls entirely inside a closed zone of one of these fractures. In the most critical configuration, one particular fracture acts as a global bottleneck, focusing all the flow through the network; it is sufficient that the closure of that fracture create a closed zone that renders its transmissivity null for the full network to be hydraulically disconnected. Less radical configurations feature the closure of more than one bottleneck on several parallel major flow paths. The identification of the disconnected networks is performed during flow simulation using the following method. Closed zones within a given fracture are allocated an aperture four orders of magnitude smaller than the mean aperture of the fracture in question. According to the cubic law (12), their local transmissivity is then twelve orders of magnitude smaller than the mean fracture transmissivity. By imposing that the precision for the numerical flow resolution be much larger (10^{-9} in practice) than the latter local transmissivity ratio, we ensure that the flow solver fails to solve the linear system for disconnected networks. In consistency with the percolation theory, the probability for a network to be connected (or connection probability) is denoted Π. The disconnection probability $1\text{-}\Pi$ is expected to increase with fracture closure.

[36] For connected networks, we compute the equivalent network permeability according to equation (16) where L is the medium linear size. As we focus here on the influence of fracture scale heterogeneities on the hydraulics at the network scale, we compare the behaviors of two networks with the same topology: one with rough fractures, the other one with parallel plate fractures. More precisely: for each studied network topology, we first simulate the flow in a configuration where heterogeneities of the local fracture apertures are taken into account, and compute the DFN's equivalent permeability K_{N+F} (the lower subscript "*N+F*" stands for "*Network+Fracture*" meaning that complexities are accounted both at the network and at the fracture scales). Equivalent permeability using Darcy's law at the network scale is computed according to:

$$K_{N+F} = \frac{Q}{L\Delta h} \tag{17}$$

where Q is the total volumetric flow through the inlet face of the domain, Δh is the head difference between the domain inlet and outlet, and L is the characteristic network size. We then simulate the flow through a network with the same topology and using the same computational mesh, but where each (rough) fracture has been replaced by a parallel plate fracture with the same (arithmetic) mean aperture. We denote K_N the corresponding equivalent permeability (the subscript "*N*" stands for "*Network*" meaning that complexity only comes from the network scale while apertures are uniform within fractures). Let us underline here that, while in the latter case the fracture local aperture fields are uniform within each fracture, so that one can assign one scalar aperture for each of them, they are not homogeneous over the population of fractures. Indeed, the fracture aperture standard deviation at scale L_c, Γ, is uniform over the medium, and so is the fracture closure $c_{\mathrm{frac}} = \sigma_a(L_f)/a_m$, where the overall standard deviation of a fracture's local aperture field $\sigma_a(L_f)$ depends on the fracture size distribution according to equation (4); thus, the

relation $a_m = \sigma_a(L_f)/c_{frac}$ imposes the variability of the mechanical apertures a_m among fractures in the DFN.

[37] We then compute the ratio of the permeabilities K_{N+F} and K_N for each DFN realization and investigate how this ratio is distributed over a large population of statistically equivalent DFNs. In this manner we filter as much as possible the first order influence of the network topology on the medium permeability, and account for the interaction between that topology and the flow localization within fracture planes. In what follows we determine the mean value for the permeability ratio over N_{SC} connected Monte-Carlo simulations as

$$\left\langle \frac{K_{N+F}}{K_N} \right\rangle = \frac{1}{N_{SC}} \sum_{t=1}^{N_{SC}} \left(\frac{K_{N+F}}{K_N} \right)_i \tag{18}$$

Note that we study the effect of fracture closure on (i) network connectivity and (ii) equivalent permeability for connected networks separately, excluding the non-connected fracture networks from the statistics of the equivalent permeability, in a manner similar to what was done in the study at the fracture scale (see section 3.1). In this study, we limit our investigations to the mean permeability ratios to obtain the general tendencies of the coupling between the fracture- and network-scale flow complexities. The variability of the permeability ratios is also of interest and deserves in itself a full study that should account for the dependence of the variability on the different fracture sizes. This could be done for example by fixing the larger fractures to focus solely on the variability of the fracture-to-network flow correlations.

3.4. Model Parameters

[38] Table 1 summarizes the model assumptions and parameters. We have chosen to normalize all dimensions by the minimal fracture size L_{fmin}. The normalization by L_{fmin} takes different meanings depending on the nature of the fracture size distribution. For networks of "infinite" fractures (LONG), the sole characteristic scale is the system size ($L_{fmin} \gg L$ and $L_{fmax} \gg L$). In the other cases (DIST and SHORT), the significant parameter is L/L_{fmin}. For fracture networks having a non-trivial fracture size distribution (DIST), enlarging the system is exactly equivalent to enhancing the fracture resolution, that is keeping L constant and lowering L_{fmin}.

[39] The choice of the size range L/L_{fmin} and of the number of Monte-Carlo simulations N_{SC} derives from a balance between the two necessities of (i) describing a reasonably large network topological complexity and (ii) sampling the permeability variability over a sufficiently large number of DFN realizations. A large number of Monte-Carlo simulations is mandatory due to the strong variability of the network topology over different realizations, especially for large distributions of the fracture sizes (DIST). The topological variability fundamentally arises from the numerous respective positions of the middle-sized fractures, which are found in limited numbers because of the power law size distribution and because the number of fractures in the network that can be handled by the simulation is also limited. To ease off this necessary trade-off between, on the one side, the number of fractures in the DFNs and the range of the described length scales, and on the other side, the number of DFN realization that are computed, we have looked for the most adapted flow numerical solvers to make it possible to solve systems of the order of 10^5 to 10^6 mesh cells in a few seconds to a few minutes at most [*Erhel et al.*, 2009a]. For these sizes of systems, the most efficient system solvers are based on the multifrontal method [*Davis and Duff*, 1999]. Thanks to this optimization, we fix $L/L_{fmin} = 10$ for LONG and DIST networks, and $L/L_{fmin} = 5$ for SHORT networks. The reason why we can afford less realizations and smaller systems in the SHORT case is that the cumulated fracture surface is much larger with more dead ends and fractures that do not effectively take part to connectivity. Thus, SHORT systems require more CPU time for the same relative density measured with respect to the percolation threshold. Let us here underline that the model studied is quite complex as it involves structures at the fracture and at the network scale that are both handled stochastically. The number of Monte-Carlo simulations ranges from 10^2 to 10^3 simulations for the denser and the sparser networks, respectively. The smaller number of simulations for the denser structures is justified by the less critical nature of the flow structure in those cases. The number of simulations was fixed by a preliminary convergence analysis that showed that results were not changed by more than 5% when doubling the number of simulations. We explore the parameter space densely and report in what follows the characteristic tendencies obtained for a subset of the simulations performed. Overall the numerical simulations performed for this study amounts to around $2\ 10^6$.

4. Results for Individual Fractures Within a DFN

[40] The case of individual fractures needed to be revisited in order to get a reference behavior at the fracture scale in the exact conditions modeled in complete "N+F" systems. Former studies have either handled different fracture aperture models or the same model on a much more restricted range of closures [*Méheust and Schmittbuhl*, 2003] or not accounted for the distribution of fracture sizes. For poly disperse systems (DIST), since the correlation length L_c is identical for all fractures, the ratio L_f/L_c depends on a particular fracture's length. This does modify the averaged connectivity and hydraulic properties of the medium. We examine the disconnection probability 1-Π and permeability ratio as defined by section 3.1 for 500 single fractures that follow the length distribution of the three fracture network types SHORT, DIST and LONG. Results are displayed in Figure 4a for $L_c = 1$ and $L_c = 3$ in the DIST case.

[41] The disconnection probabilities 1-Π (Figure 4a) logically increases while increasing the fracture closure c and/or the aperture correlation scale L_c, as both effects result in extending the area of the closed regions of the fracture plane 1-Π follows the average proportion of closed regions in a fracture's plane.

[42] Disconnection occurs preferentially in the fractures of size smaller or around the correlation scale L_c because, for these fractures, correlations exist in the aperture field up to the scale of the fracture length, so that a single closed region of the fracture plane extending throughout the fracture may by itself disconnects it. Fracture disconnection might thus occur either by reducing the fracture lengths (shift from DIST to SHORT type of fracture length distribution) or by enlarging L_c, which is in effect the cut-off length controlling the size of the closed regions.

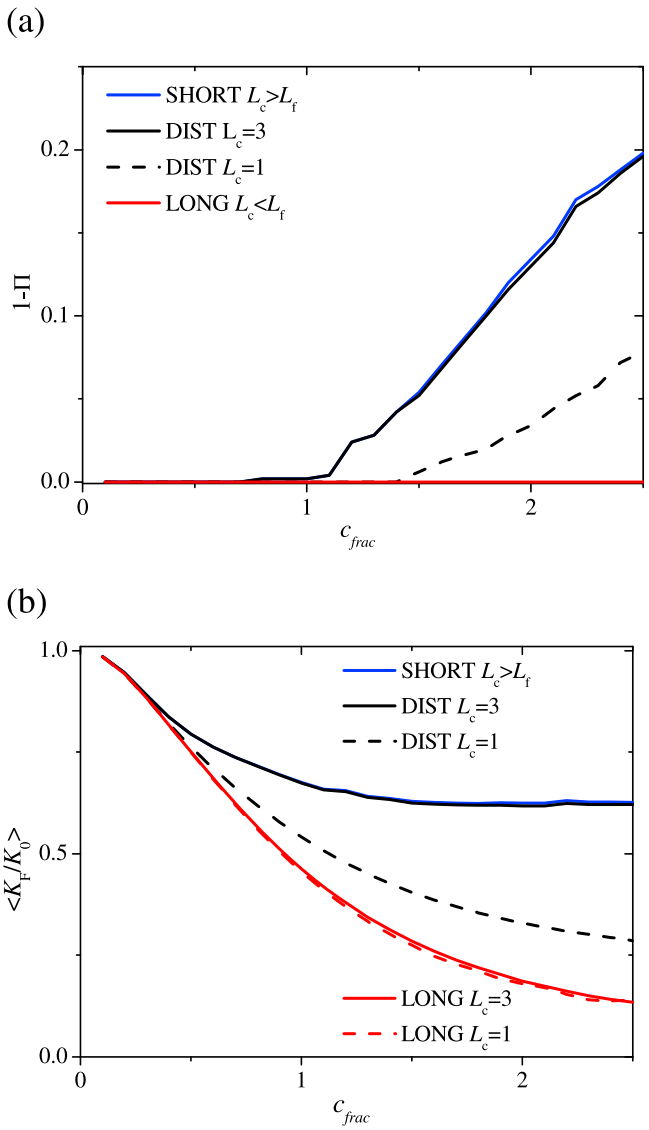

Figure 4. (a) Fracture-scale disconnection probability 1-Π and (b) average permeability ratio $\langle K_F/K_0 \rangle$. When not indicated, values are valid for all values of L_c larger than 1.

[43] $\langle K_F/K_0 \rangle$ varies consistently with 1-Π (Figure 4b). It goes to 1 at infinitely small closure c_{frac} (i.e., when the local transmissivity distribution vanishes) and decreases monotonically with the fracture closure, while the variability steadily increases. As $\langle K_F/K_0 \rangle$ is always smaller than 1, distributed apertures always reduce the equivalent permeability compared to the parallel plate behavior. This effect results from the variability of the flow channeling inside the fracture plane. It is in particular controlled by the orientation toward the average flow of the channels with the largest local transmissivities [*Méheust and Schmittbuhl*, 2001]. Configurations detrimental to flow being more numerous than those enhancing flow, permeability is reduced on average. Flow reduction is enhanced by larger L_c values. These results are consistent with the ones previously acquired by *Méheust and Schmittbuhl* [2001, 2003], complement them on a fuller range of closure values. For the DIST case, they also quantitatively differ because of the L_f/L_c variability induced by the fracture size distribution.

5. Results for Full Fracture Networks

[44] We are reporting the effect of both fracture aperture and fracture network properties by systematically varying the fracture closure c, the cutoff length L_c, the type of fracture size distribution (SHORT, DIST, LONG) and the density of fractures in the network, p/p_c. Beyond the systematic characterization of connectivity and effective permeability, we seek a better understanding of the interactions between fracture-scale heterogeneities and network-scale topology by comparing the fracture-scale and network-scale results.

5.1. Disconnection Probability

[45] Disconnection at the network scale (Figure 5) follows the same tendency as at the fracture scale (Figure 4a). Disconnection grows monotonously with the closure c_{frac}. The disconnection probability is a more pronounced phenomenon at the network scale, because closed areas do not have to extend across whole fracture planes for the network to lose its connectivity, but it is sufficient for them to just close the bottle necks of the connectivity structure. Consequently, the disconnection probability 1-Π is significant for DFNs that are close to the percolation threshold, and sharply decreases as the density of fractures is increased (Figure 5, squares compared to disks), since a larger number of potential paths are then made available. For DFNs with a larger density, the disconnection rate becomes even lower at the network scale than at the fracture scale because of the existence of parallel connected paths that cannot be all disconnected by closed areas. This phenomenon is even more marked for SHORT than for DIST networks (Figure 6b compared to Figure 6a) as the number of connected paths increases faster with density for smaller fractures (with the measure of density given by equation (2)).

[46] Because of the finite size of the systems studied, the latter analysis will likely hold for DIST networks but is incomplete for SHORT networks at threshold. In fact, for DIST networks, fractures forming the connected structures range over a limited size interval [*de Dreuzy et al.*, 2001c; *Wellman et al.*, 2009]. Increasing the system size or equivalently enhancing the system resolution will not issue dramatic changes in the system connectivity, but rather add smaller fractures to the existing main connected paths. On the contrary, for SHORT networks at the percolation threshold, increasing the system size results in enlarging the number of fractures that are essential to network connectivity; indeed, the number of these links scales as L^{d_R} with $d_R = 1.14$ in 3D systems [*Stauffer and Aharony*, 1992]. As the system size is increased more and more, the probability that breaking just one of these links might disconnect the whole network increases to 1. For SHORT networks that are lying above the percolation threshold, this situation is not to be encountered as long as the typical distance between two independent paths, also called the correlation length in the percolation theory terminology (but not to be confused with the our correlation length L_c), is smaller than the system size.

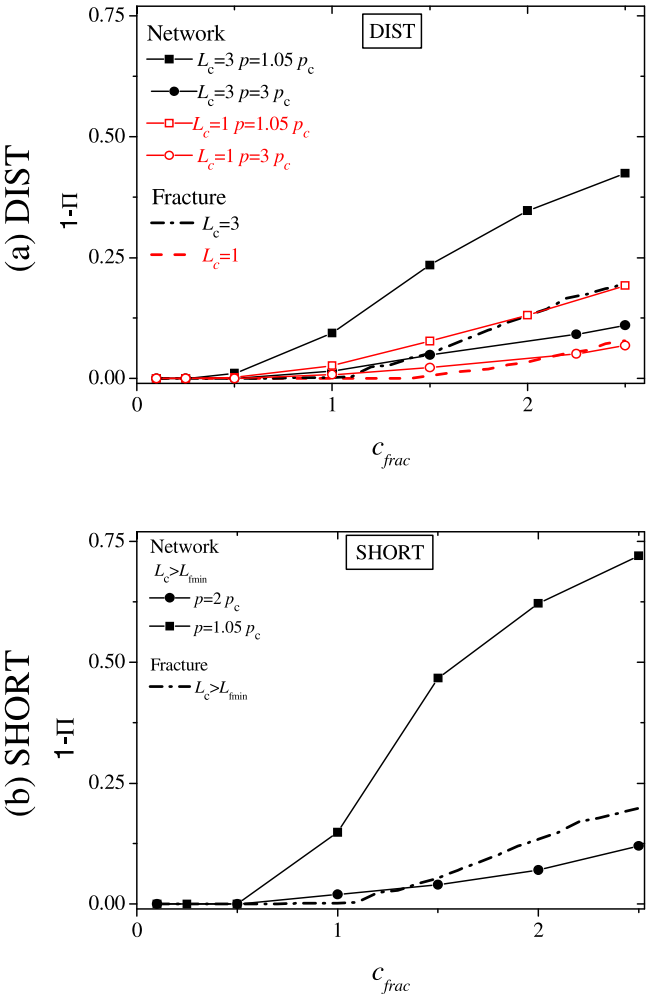

Figure 5. Network-scale disconnection probability for SHORT and DIST networks. LONG networks never become disconnected. Note that the vertical scale has been chosen to be equal in both graphs.

5.2. Mean Permeability Ratio $\langle K_{N+F}/K_N \rangle$

[47] The behavior of the mean permeability ratio $\langle K_{N+F}/K_N \rangle$ as a function of the medium closure is illustrated in Figure 6. Larger values close to 1 indicate a restricted effect of heterogeneous fracture aperture distributions, while values deviating from 1 indicate on the contrary that taking heterogeneities below the fracture scale into account in the model changes the DFN's hydraulic behavior significantly. $\langle K_{N+F}/K_N \rangle$ is also always smaller than 1, at least in the density range studied here. It means that the local fracture aperture distribution reduces the equivalent network permeability systematically. In addition, $\langle K_{N+F}/K_N \rangle$ ranges between 0 and 1 covering almost all possible values, and systematically decreases as a function of the closure c_{frac}. This effect first comes from the influence of the aperture distribution at the fracture scale itself, measured by $\langle K_F/K_0 \rangle$ (see section 4). $\langle K_{N+F}/K_N \rangle$ and $\langle K_F/K_0 \rangle$ do in fact display very similar tendencies as functions of the fracture closure c_{frac} (Figure 6, thick lines compared to line and symbols plots of the same color). However, they differ quantitatively, except in few cases like for the distributed fracture length networks DIST with L_c = 1 at p/p_c = 3, and the long fracture networks LONG with L_c = 1 at p/p_c = 1.05.

[48] These two specific cases occur at highly different fracture densities. In the second case (long fractures), the equality is expected because, networks that are close to the percolation threshold consist of almost a unique fracture.

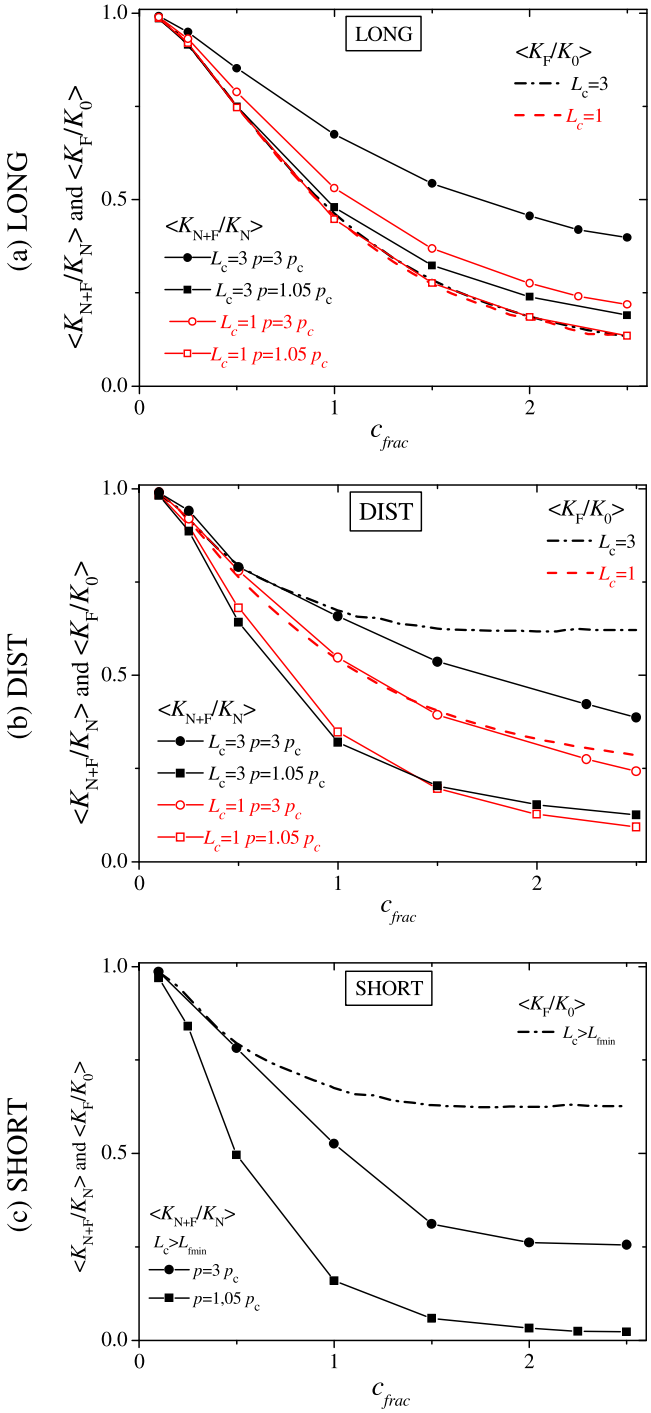

Figure 6. Network- and fracture-scale permeability ratios. Each point represents an average over 10^2 and 10^3 simulations for the denser and sparser cases respectively.

A small difference between the network scale and the fracture scale occurs because of the possible connection by 2 to 3 diagonal fractures in series rather than 1 fracture in some configurations. These differences are negligible for system sizes L much larger than the cut-off length L_c.

[49] In most cases, the fracture and network scale permeability ratios differ significantly. There exists both configurations for which the network scale permeability ratio is smaller than its fracture scale counterpart, and configurations for which it is larger. When $\langle K_{N+F}/K_N\rangle > \langle K_F/K_0\rangle$, two effects compete: aperture heterogeneities below the fracture scale tend to decrease the medium permeability, while the network topology tends to increase it by allowing the fluid to select a path through the most transmissive fractures. For example in the LONG case above percolation threshold (Figure 6a), networks are made up of a superposition of long fractures, each of them almost extending through the whole domain. Taken individually, they would lead to a permeability ratio identical to that at the fracture scale. Taken together, they intersect themselves and offer additional larger transmissivity shortcuts and deviations, enhancing thus the equivalent network permeability.

[50] On the contrary, for the SHORT networks made up of small fractures (Figure 6c), the effect of the network is to reduce the equivalent permeability ($\langle K_{N+F}/K_N\rangle < \langle K_F/K_0\rangle$) in complete consistency with the previously reported effect on the disconnection rate (see section 5.1). These connected networks made up of small fractures have the most complex topology. Close to the percolation threshold, they display a large number of bottle necks, which are expected to be highly sensitive to local apertures within fracture planes. A small reduction of the aperture around these bottle necks will strongly reduce the full network permeability, while a large enhancement of the permeability of the same zones will only slightly increase the network permeability. The permeability ratio reduction can be quite large around the percolation threshold where $\langle K_F/K_0\rangle$ tends to 0.5 while $\langle K_{N+F}/K_N\rangle$ tends to 0. If that reduction is less marked above the threshold, for which bottle necks are rarer, it is still very well marked and can be explained within the framework of critical path analysis [*Ambegaokar et al.*, 1971; *Charlaix et al.*, 1987; *Hunt and Gee*, 2002]. Above the percolation threshold, small apertures acting as bottle necks lower the permeability of the whole path to which they belong. Increasing the fracture density means increasing the number of alternative paths and progressively removing the limitations induced by smaller fracture apertures by allowing them to be bypassed.

[51] The length-distributed configurations (DIST) display a richer range of behaviors, with network-scale permeability ratios smaller than their fracture-scale counterpart around the percolation threshold (p/p_c = 1.05), as for the SHORT case (Figure 6b, squares), but of same magnitude for higher densities p/p_c = 3 and L_c = 1, as for the LONG case (Figure 6b, red circles). Around the percolation threshold, $\langle K_{N+F}/K_N\rangle$ is not affected by L_c and tends to be controlled essentially by the fracture network topology and the fracture closure c_{frac} and not by the repartition of apertures within the fractures (L_c), once the network has proven to be connected. In other words, for DFNs at the percolation threshold, L_c mostly influences the disconnection rate 1-Π but not the permeability ratio of the connected networks. If closed areas do not cover the network bottle necks, their relative extension within the fracture does not influence the network transmissivity. Flow equally bypasses these closed zones whatever their extension as long as they do not disconnect the network. While the equivalent permeability is not much altered, flow structures within the network vary consequently as shown by Figure 3. These variations concern both the fracture scale and the network scale. Aperture-scale heterogeneity tend to modify the circulation pattern within the fracture because of constraints imposed by the neighboring fractures. This is shown in Figure 7, which compares flows in a given fracture at two different fracture closures c_{frac} equal to 0.25 (Figure 7, left) and 1 (Figure 7, right) within the network displayed in Figure 3. The thick black segments identify the intersections of the fracture plane with the neighboring fractures. The comparison of the flow and head fields (Figures 7 (middle) and 7 (bottom)) shows that when aperture heterogeneity is present in the fracture, the flow is partly re-directed to the top left side of the fracture (from left to right in Figure 7) and that this re-direction cannot be explained by the local transmissivity structure (Figure 7, top). In fact the right side of the fracture remains hydraulically well connected.

[52] Above the percolation threshold, percolation is less critical, and the effective permeability becomes sensitive to the mean medium permeability, and consequently to the cut-off scale of the aperture correlation pattern (Figure 6b, red circles compared to black disks).

5.3. Permeability Correction Factor

[53] As shown in the previous section, $\langle K_{N+F}/K_N\rangle$ and $\langle K_F/K_0\rangle$ display similar tendencies as a function of fracture closure c_{frac}. The same kind of similarity is displayed both for aperture cutoff scales L_c and network topologies (density and length distribution). Based on this similarity, and depending on whether the network permeability is reduced or enhanced by the fracture aperture distribution, we define the correction factor α:

$$\begin{aligned} &\text{if } \frac{\left\langle \frac{K_{N+F}}{K_N}\right\rangle}{\left\langle \frac{K_F}{K_0}\right\rangle} > 1 \quad \text{then} \quad \alpha = \frac{\left\langle \frac{K_{N+F}}{K_N}\right\rangle}{\left\langle \frac{K_F}{K_0}\right\rangle} - 1 \\ &\text{otherwise} \quad \alpha = 1 - \frac{\left\langle \frac{K_F}{K_0}\right\rangle}{\left\langle \frac{K_{N+F}}{K_N}\right\rangle} \end{aligned} . \tag{19}$$

The absolute value of α is a measure of how much the typical ratio of the permeability of the full fracture network to that of the corresponding parallel plate fracture network differs from the typical permeability ratio of a single rough fracture within the network to the corresponding parallel plate fracture; $\alpha < 0$ when the network structure induces a reduction of the permeability compared to the equivalent fracture transmissivity. Conversely $\alpha > 0$ when permeability is enhanced. Note that equation (19) defines $\langle K_{N+F}/K_N\rangle/\langle K_F/K_0\rangle$ as continuous for $\langle K_{N+F}/K_N\rangle = \langle K_F/K_0\rangle$. The correction factor α can take all possible negative values as $\langle K_{N+F}/K_N\rangle$ can tend to zero for hardly connected networks. α is however bounded above by the ratio of the maximum local transmissivity to the minimum one, minus 1. Although not providing any new information with respect to $\langle K_{N+F}/K_N\rangle$ and $\langle K_F/K_0\rangle$, α demonstrates

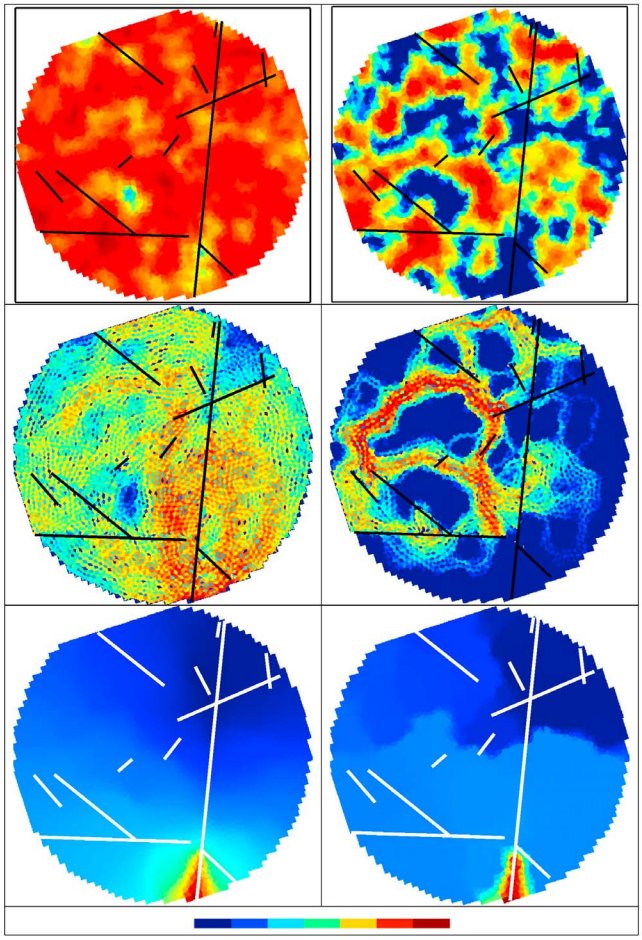

Figure 7. (top) Log-permeability fields, (middle) logarithm of the flow fields, and (bottom) head fields in one of the large fractures of the DIST network shown in Figure 1 at fracture closures (left) $c_{\mathrm{frac}} = 0.25$ and (right) $c_{\mathrm{frac}} = 1$; the correlation length is $L_c = 1$. The traces of the intersections with the other fractures are represented as black linear segments superimposed on the permeability and flow fields. Color scales are all relative to the minimum ($x_{\min}$) and maximum ($x_{\max}$) of the quantity (x) represented. Colors are matched to the corresponding quantity on a continuous scale where the discrete values $x_{\min} + k/6\,(x_{\max} - x_{\min})$, for $0 \le k \le 6$, correspond respectively to the following colors: navy ($k = 0$), blue ($k = 1$), cyan ($k = 2$), green ($k = 3$), orange ($k = 4$), red ($k = 5$), and purple ($k = 6$), shown at the very bottom of the figure. Note that the small-scale color variability of the flow field (Figure 7, middle) comes from the representation of the norm of the flow field averaged over the edges of each mesh cell.

several essential features of the effect of the network structure on the upscaling of local transmissivity distributions. First, α ranges over a wide interval between -31 and $+2$ (Figure 8). Except for networks of long fractures or very dense networks, the network topology generally induces a reduction of permeability rather than an increase. Second, α is monotonic as a function of the fracture closure c_{frac}. For given assumptions for the fracture and network structures (fixed length distribution, L_c and p/p_c), α is either monotonically increasing, monotonically decreasing or steadily zero. Third, the variations of α are rather quadratic than linear, which implies a strong impact of fracture closure on the reduction and enhancement factors. The systematic similarity between fracture- and network-scales variations previously evoked

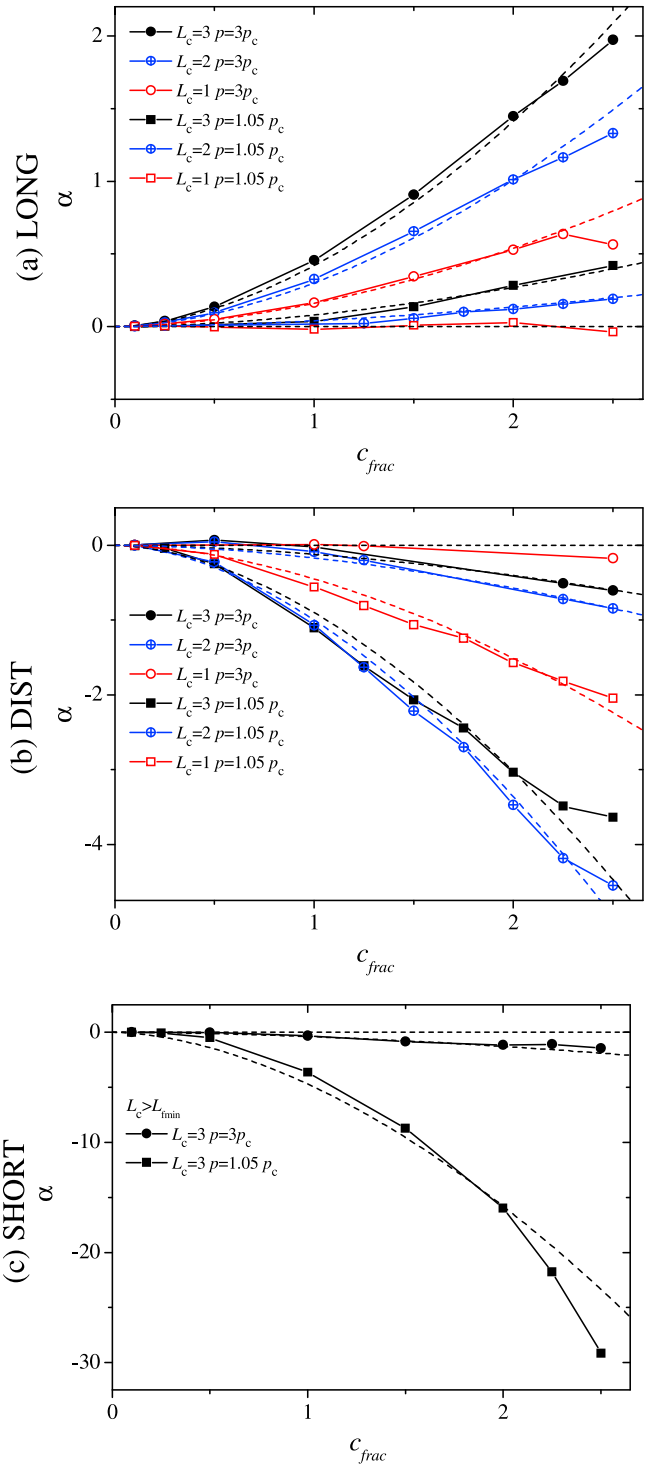

Figure 8. Permeability enhancement and reduction factors $\alpha+$ and $\alpha-$ as functions of fracture closure c for different values of fracture density p/p_c and cut-off scale L_c. The dashed line next to the data plot represents the closest power law tendency: $c_{\mathrm{frac}}^{1.75}$.

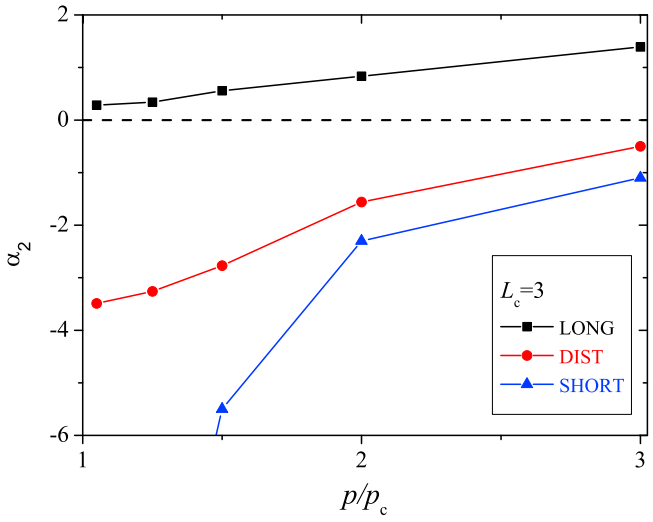

Figure 9. Characteristic permeability correction factor α_2 as a function of the fracture density relative to the percolation threshold.

translates to the variations of α as a function of the fracture closure c_{frac}. Moreover the scaling tendency appears to be very close to $c_{\text{frac}}^{1.75}$ (dashed line compared to data point). Deviations are generally less than 5% and do not go over 10%, which is quite remarkable given the simplicity of the power law model. The case relevant to percolation theory at threshold should be set aside as already discussed in section 5.1. Thus α may be approximated by:

$$\alpha(c_{\text{frac}}) \approx \alpha_2 \left(\frac{c_{\text{frac}}}{2}\right)^{1.75} \tag{20}$$

where we have chosen to relate the characteristic amplitude of α to its value $\alpha_2 = \alpha(c_{\text{frac}} = 2)$.

6. Discussion

[54] The correction factor α may be interpreted as the correction that should be applied to the network permeability by using equations (19) and (20), to account for aperture distributions within fracture planes, without modeling them explicitly:

$$\begin{aligned} &\text{if } \alpha > 0 \text{ then} && \langle K_{N+F}\rangle = \langle K_N\rangle \left\langle \frac{K_F}{K_0}\right\rangle \left(1 + \alpha_2 (c_{\text{frac}}/2)^{1.75}\right) \\ &\text{otherwise} && \langle K_{N+F}\rangle = \langle K_N\rangle \left\langle \frac{K_F}{K_0}\right\rangle \frac{1}{\left(1 - \alpha_2 (c_{\text{frac}}/2)^{1.75}\right)} \end{aligned} . \tag{21}$$

α_2 can be considered to fully characterize the interaction between fracture and network scale heterogeneities. When $\alpha_2 = 0$, the full medium permeability can be directly written as the network permeability times the mean equivalent fracture permeability ratio $\langle K_{N+F}\rangle = \langle K_N\rangle\langle K_F/K_0\rangle$. In other word, fracture-scale and network-scale effects on the equivalent permeability are completely decoupled in this case. Such a situation occurs for example when networks are made up of a small number of long fractures (LONG) with a cut-off scale sufficiently small compared to the system scale. This is typically a situation where homogenization is expected to be closely verified. When density increases, α_2 becomes positive as the network structure can offer bypasses to some of the smallest permeability areas. In most cases, the correction (21) should be applied to the simple decomposition into network-scale and fracture-scale permeabilities.

[55] We interpret α_2 as the upscaling parameter characterizing the effect of the network topology on the upscaling of permeability, from its fracture scale measure and up to the DFN's equivalent permeability in the same spirit as the power-averaging exponent ω [*de Dreuzy et al.*, 2010; *Desbarats*, 1992; *Renard and de Marsily*, 1997; *Ronayne and Gorelick*, 2006]. ω was initially defined to describe in a compact way the upscaling law for a lognormal distribution of local permeabilities as a function of the Euclidean dimension of the embedding space [*Desbarats*, 1992; *Matheron*, 1967]. ω ranges between -1 (harmonic average) and 1 (arithmetic average), corresponding respectively to a purely system in series and a purely parallel system. Upscaling in 1D is performed by the harmonic mean ($\omega = -1$), in 2D by the geometrical mean ($\omega = 0$), and in 3D it is very close to $\omega = 1/3$. A non integer value like 1/3 indicates that the organization of the flow paths occurs more in parallel than in series and that the upscaling can be straightforwardly expressed as a well-defined composition of the arithmetic and geometric average. α_2 and ω operate on different types of local permeability distributions, which are the lognormal distribution for ω and a truncated Gaussian for α_2, as well as by their range of variations: while ω is limited in the interval $[-1, 1]$, α_2 can take a much larger range of values. But one can draw a formal analogy between them along the two following lines: (i) They both express upscaling laws in a compact way. When ω and α_2 are negative, upscaling results in permeability decrease, and conversely when ω and α_2 are positive. (ii) Most importantly, they do not depend on the magnitude of the local permeability distribution (c_{frac} here, for α_2), but only on the structural properties of the system such as the Euclidean dimension for ω and the topological structure of the fracture network for α_2. (iii) When $\langle K_{N+F}/K_N\rangle > \langle K_F/K_0\rangle$, α_2 is positive and the organization of fluxes among various fractures is more in parallel than in series, as when ω is positive, so that on the one hand the network structure enhances the effective permeability from fracture to network scale, and on the other hand the system permeability will typically be sensitive to the mean medium properties (fracture density, cut-off scale). Conversely, when $\langle K_{N+F}/K_N\rangle < \langle K_F/K_0\rangle$, α_2 is negative and the organization of fluxes is more in series than in parallel, as is the case when ω is negative. Consequently, the network structure then reduces the effective permeability from the fracture scale to the network scale, and the system permeability will be more sensitive to local values of permeabilities and especially to those around connectivity constrictions. In summary, α_2 is a quantitative measure of how the two competing effects previously observed in section 5.2 balance each other; it offers an alternative to ω for these types of local permeability distributions that are properly described neither by harmonic averages, nor by geometric averages.

[56] Going more into details, we relate the variations of α_2 to key geometrical characteristics of the fracture and network structures. First, when α_2 is positive, it increases monotonically with the fracture density whatever the type of fracture length distribution (Figure 9). Higher fracture densities offer

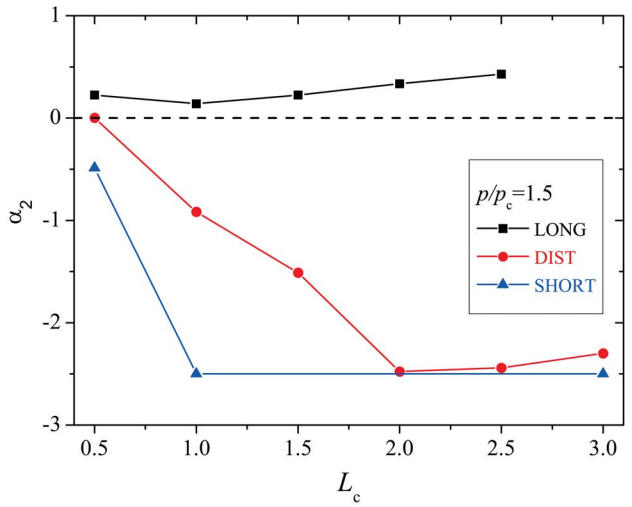

Figure 10. Characteristic permeability modification factor α_2 as a function of the cutoff scale L_c.

more parallel paths that can act as alternatives to paths that necessarily contain small local permeabilities. At the fracture scale, high transmissive areas of typical size L_c may fully bridge the characteristic flow distance within the fracture. We shall denote this scale d_I. On the flow structure presented in the right middle row of Figure 7, d_I would be taken as the mean distance between fracture intersections (thick black segments) along the main flow channels. If this definition is conceptually intuitive, a proper derivation of d_I would be difficult. It is however straightforward that d_I is inversely proportional to the fracture density and that the bridging effect previously described depends on the ratio L_c/d_I. The increase of L_c/d_I promotes the development of highly permeable paths that exploit only the high permeability zones of the fractures. This is a typically a positive correlation effect on the global flow between the fracture- and network-scales.

[57] Sections 5.1 and 5.2 have revealed the existence of another effect linked to the lengths of the fracture intersection. Fracture intersections falling into closed areas have a major effect on the connection probability at the percolation threshold. If this effect is minor on the permeability of DFNs that are at the percolation threshold, it becomes more important for those that are above threshold, because it induces hydraulic disconnection of otherwise geometrically connected paths. The induced permeability reduction depends on the ratio of the mean fracture intersection length l_I to the cutoff-scale L_c. Both effects cumulate in the DIST case while only the second one is active in the LONG case, which explains the stronger impact of the fracture density on α_2 in the DIST case (Figure 9).

[58] Both effects may however lead to different sensitivity of the correction factor α_2 to the cutoff length L_c, as evidenced in Figure 10. For DFNs of type SHORT (blue triangles), the sharp reduction of permeability when the fracture length becomes larger than the cut-off length L_c comes from the second disconnecting effect (decrease of l_I/L_c). It also dominates in DFNs of type DIST for $L_c < 2 = L/5$ (Figure 10, red disks). In this case, which is the most realistic with respect to modeling a geological medium, α_2 decreases regularly to nearly 0 as L_c is decreased to 0.5 = L/20. This means that if the medium size is 20 times larger than the correlation length, the coupling between fracture-scale and network-scale flow heterogeneities is weak. For these DIST configurations and for $L_c > 2$, in contrast, variations are reversed with a slight but genuine increase of α_2 that is likely to be due to the first bridging gap effect controlled by L_c/d_I. For DFNs of type LONG, α_2 mostly increases, also as a consequence of the "bridging gap" effect (Figure 10, black squares).

[59] The disconnecting effect highlights the importance of the correlation between the aperture field and the position of the fracture intersections within the corresponding fracture plane. Larger apertures at fracture intersections might sharply enhance network permeability and should be investigated using the available experimental means [e.g., *Detwiler et al.*, 1999; *Pyrak-Nolte and Morris*, 2000]. The bridging gap effect highlights the importance of the fracture network structure, and in particular of its correlation pattern. The spatial distribution of the fracture centers is not Poissonian [*Bour and Davy*, 1999; *Darcel et al.*, 2003a]. The mechanical constraints imposed externally on and induced internally by fracture intersections generate more complex correlation structures that result in relatively dense but poorly connected networks [*Davy et al.*, 2010]. Under those assumptions, which are more complex than the ones upon which we have based the present study, the flow distribution is expected to be broader and the hydraulically active scale between fracture intersections, d_I, to be strongly influenced accordingly.

7. Conclusions

[60] We have developed a model to study the combined effect of fracture scale heterogeneity and network topology on the equivalent permeability of a fractured medium. At the fracture scale, local apertures are distributed according to a truncated Gaussian distribution and spatially correlated according to a self-affine pattern with an upper cutoff scale L_c. The ratio of the local aperture variance to its mean, denoted as the fracture closure c_{frac}, is the key parameter that controls the heterogeneity of local permeabilities at the fracture scale. At the network scale, the network topology is described both by a fracture length distribution and by a fracture density. We have considered a wide range of densities, ranging from sparse networks close to the percolation threshold to dense networks well above the threshold, and various networks with highly differing topologies, consisting either of fractures much smaller than the network scale L, much longer than L or of a full distribution of fracture sizes between $L/10$ and L. Flow simulations were performed first on single fractures to obtain a reference for permeability upscaling and second at the network scale using numerical methods that account for complex three-dimensional network geometries. Because of the numerous sources of complexity, we performed an extensive sampling of the parameter space with 100 to 1000 Monte-Carlo replicas for each parameter set, which amounts to around two million simulations altogether. We have also set up a methodology that optimizes the analysis of the combined effect of the fracture- and network-scale complexity by systematically comparing the same network structures with and without heterogeneity in the local fracture apertures (i.e., fracture wall roughness).

[61] At the fracture scale, we have shown that the distribution of local apertures systematically induces a reduction

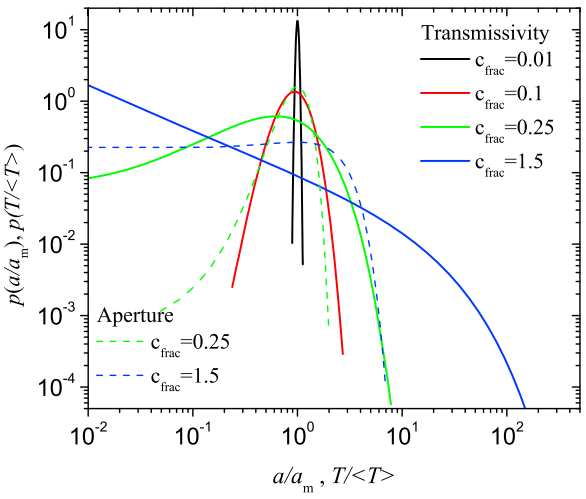

Figure A1. Aperture- and transmissivity- distributions within a fracture shown as dashed and solid lines, respectively, for various levels of fracture closure.

of the mean equivalent permeability because of the higher probability of generating obstacles than channels, in full consistency with previous studies performed for narrower ranges of heterogeneities [*Méheust and Schmittbuhl*, 2000, 2003]. The maximum reduction of the mean equivalent permeability remains limited to a factor of 2 to 6, depending mostly on the ratio of the fracture scale to the self-affinity cutoff scale, while the local transmissivity distribution spans several orders of magnitude. The restricted range covered by the reduction of equivalent permeability compared to the widely distributed local transmissivities is a remarkable property of the fracture transmissivity field.

[62] At the network scale, the equivalent permeability was found to be either larger or smaller than its fracture scale counterpart. By systematically studying the network-scale permeability with reference to the permeability of the corresponding network of parallel plate fractures, we investigated the cumulative effect of fracture heterogeneity and network topology. For most of the configurations studied, the permeability of a network consisting of rough fractures cannot be simply obtained as the product of (i) the permeability of a network consisting of the same fractures but without any wall roughness and (ii) a correction factor accounting for the typical permeability reduction of a single fracture when taking its local aperture heterogeneities into account. In other words, there is a significant coupling between flow heterogeneities at the fracture scale and flow heterogeneities at the network scales. A consequence of that coupling is that for a given network topology, in many cases, the DFN's equivalent permeability will not be properly predicted by a simulation where each fracture is modeled as a parallel plate with a given permeability. However, when the system size is larger than about 20 times the correlation length L_c, this coupling is found to be weak; for a correlation length given as a property of the rough fractures, this fixes the range of system sizes for which it is important to take fracture scale heterogeneities into account: at very large scales, DFNs of parallel plates with the proper hydraulic aperture distribution are a proper hydraulic description of the fractured medium.

[63] The enhancement or reduction of the impact of fracture wall roughness on permeability when upscaling from the fracture scale toward the network scale is measured by the correction factor α, which means that α quantifies the above mentioned coupling. Enhancement is found to occur for dense systems and for network of long fractures. Reduction occurs for networks that are closer to the percolation threshold and for network of small fractures. The correction (either enhancement or reduction) factor α appears to depend on the fracture closure c_{frac} according to a power law dependence of exponent close to 1.75. Thanks to this simple dependence, flow upscaling from the fracture-scale up to the network scale can be fully characterized by the correction factor α_2, defined as the enhancement or reduction factor α at $c_{\text{frac}} = 2$. α_2 is a quantitative measure that is analogous to the more classical power-averaging exponent ω in this case, for which the local transmissivity distribution neither has a harmonic average nor a geometric average. A systematic analysis of α_2 as a function of the model parameters showed that the flow upscaling is governed by two competing effects. On the one hand, the network permeability is lowered by the disconnection effect that consists in fracture intersections falling inside closed or low transmissive areas. The permeability reduction increases with the ratio of the characteristic distance between intersections within the flow structure to the aperture cutoff scale. On the other hand, the network permeability is enhanced by the existence of high permeability zones within the fractures that can bridge the portion of a fracture plane between intersections with hydraulically active fractures. The permeability enhancement then increases with the ratio of the cutoff scale L_c to the characteristic distance between fracture intersections.

[64] In further studies, we plan to extend our investigations to other controlling factors including shear displacement of the fractures, which results in a fracture-scale permeability anisotropy that is potentially correlated to the fracture orientation; more generally we shall study how an anisotropic mechanical load impacts the permeability of the entire medium through its effect on fracture-scale heterogeneity.

Appendix A: Illustration of Local Aperture and Transmissivity Distributions

[65] Figure A1 displays the distribution of aperture normalized by its mechanical aperture, $a_m = \sigma_a/c_{\text{frac}}$, and the distribution of local transmissivities T, normalized by its characteristic value $\langle T\rangle = \beta a_m = \beta(\sigma_a/c_{\text{frac}})^3$. It appears that the relative transmissivity distribution (solid lines) is much wider than the aperture distribution (dashed lines) for not too small values of c. For c approximately larger than 1, the transmissivity distribution is a power law of exponent $-2/3$ truncated by a fast decreasing exponential as shown by equation (8). Because the power law exponent is larger than -1, the mean and standard deviation of the relative positive permeability values $\mu(T/\langle T\rangle)$ and $\sigma(T/\langle T\rangle)$ are dominated by the larger normalized permeability values (Figure A2), where $\langle T\rangle$ is the average value of the truncated transmissivity distribution. It explains the strong increase of the transmissivity distribution's width with c_{frac} (Figure A1). The standard deviation of the aperture distribution becomes larger than its mean when c_{frac} becomes larger than about 0.35. The mean

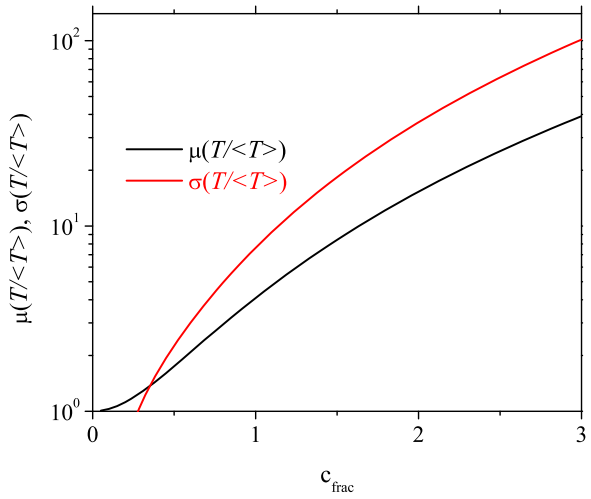

Figure A2. Mean and standard deviation of the local truncated fracture transmissivity distribution as a function of the a priori fracture closure c_{frac}.

and standard deviation increase by one and a half to two orders of magnitude for c_{frac} ranging from 0.35 to 2.5.

Appendix B: Fracture Network Generation

[66] In order to generate random DFNs, with various probability laws modeling the geometry and the physical properties, we developed a specific tool [*Erhel et al.*, 2009b, 2011], with streams of random numbers generated by the RngStream package [*L'Ecuyer et al.*, 2002], and input and output parameters described in XML files. This generic tool allows also running multiparametric simulations with a large number of samples. It provides simulation results for each sample as well as statistical results. The software MP_FRAC uses this tool extensively, whereas computational geometry is handled by the CGAL package (CGAL, Computational Geometry Algorithms Library, http://www.cgal.org). Currently, MP_FRAC can simulate steady state flow with various types of boundary conditions.

[67] The simulation domain has been set to a cube of edge length L. Fracture centers are generated within the domain uniformly by imposing uniform distributions of their coordinates in the three directions. The power law fracture length distribution is sampled by the inverse probability integral transform, which consists in sampling and then inverting the cumulative probability distribution. The orientation distribution of fracture normal vectors is generated by the rejection sampling method. Points are uniformly generated in a unit cube, accepted if within the unit sphere and then projected on the sphere to give the direction normal to the fracture plane [*de Dreuzy et al.*, 2000].

Appendix C: Fracture Aperture Distributions

[68] The aperture field for each fracture is generated on a square grid, in the Fourier domain: its Fourier transform is defined as $\tilde{a}(\mathbf{k}) = \sqrt{S(k)}\,\exp(i\varphi(\mathbf{k}))$, where $S(k)$ is a power spectrum in the form expressed by equation (5) and $\varphi(\boldsymbol{k})$ is a phase that is drawn randomly from a uniform distribution on the $[0; 2\pi]$ interval for all wave vectors pertaining to one half of the Fourier space, and set to $\varphi(\mathbf{k}) = -\varphi(-\mathbf{k})$ on the other half. The random phase definition ensures that the inverse Fourier transform, a, of the complex function $\tilde{a}$ be real in the space domain.

[69] At this point, the mean value of the aperture field is subtracted from it, and the whole field is scaled so as to ensure an overall standard deviation as defined by equation (4). It is then added a constant shift corresponding to the desired mechanical aperture $a_m = \sigma_a/c_{frac}$. Finally, all negative values of the local apertures are set to a very small value. That very

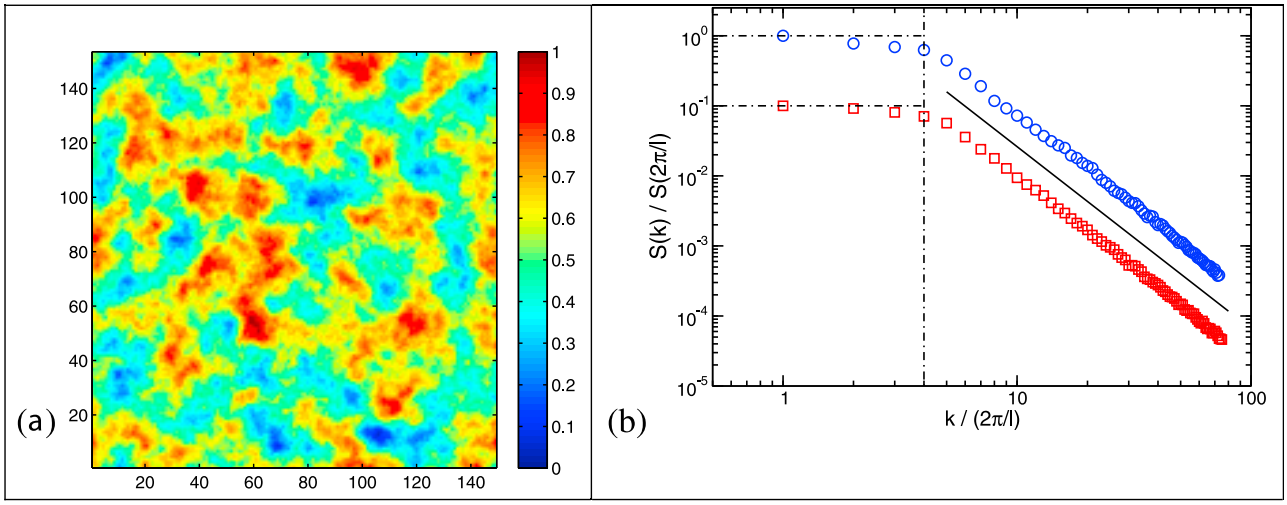

Figure C1. (a) Local aperture field within a large fracture for which the correlation length L_c is a fourth of the fracture size L_f. The relative closure is $c_{frac} = 1/4$ so that no closed region exists in the fracture plane; the aperture field has been normalized by its largest local maximum value. (b) Corresponding average power spectral densities of horizontal (in blue) and vertical (in red) topographic profiles; the red plot has been scaled by a factor 1/10 for clarity; the black solid line represents a power law behavior of exponent −2.60, corresponding to a Hurst exponent $H = 0.80$.

small value is chosen differently depending on the type of simulations that are performed: in the study of the permeability at the fracture scale (section 4 below) the aperture of the closed zones is set to the mean aperture divided by 10^{10}; for the flow simulation in the full DFN network (section 5), it is set to the mean aperture divided by 10^4. Figure C1a provides a representation of such an aperture field ($L_c = L_f/4$ and $a_m = 4\sigma_a$), in which the colormap is mapped to local apertures: there is hardly any closed region in that case (c_{frac} = 0.25) of the fracture plane appear in dark blue while the largest local aperture appears in bright red. It appears clearly on the topographic map that correlated low- or high- aperture regions do not extend along the fracture plane over lengths larger than L_c. The corresponding spectral densities for horizontal and vertical profiles of the topography, averaged over all profiles, are shown in Figure C1b; they agree well with equation (5), which validates the generation scheme.

[70] In the network simulations, the aperture field of a given fracture is first generated on a fine square grid and then interpolated on the triangular unstructured mesh of the fracture within the network. The square grid step is chosen twice finer than the triangle characteristic scale, and averaging of apertures is performed over the grid cells of the regular grid embedded within each triangle.

[71] **Acknowledgments.** J.-R. de Dreuzy acknowledges the European Union for its additional funding through the IEF Marie-Curie fellowship (PIEF-GA-2009-251710). Additional funding was provided by the French National Research Agency ANR through the H2MNO4 project for the development of simulation methods (ANR-MN-2012-).

References

Acuna, J. A., and Y. C. Yortsos (1995), Application of fractal geometry to the study of networks of fractures and their pressure transient, *Water Resour. Res.*, *31*(3), 527–540, doi:10.1029/94WR02260.

Ambegaokar, V., et al. (1971), Hopping conductivity in disordered systems, *Phys. Rev., B, Solid State*, *4*(8), 2612–2620, doi:10.1103/PhysRevB.4.2612.

Baghbanan, A., and L. R. Jing (2007), Hydraulic properties of fractured rock masses with correlated fracture length and aperture, *Int. J. Rock Mech. Min. Sci.*, *44*(5), 704–719, doi:10.1016/j.ijrmms.2006.11.001.

Balberg, I., et al. (1984), Excluded volume and its relation to the onset of percolation, *Phys. Rev. B*, *30*(7), 3933–3943, doi:10.1103/PhysRevB.30.3933.

Barker, J. A. (1988), A generalized radial flow model for hydraulic test in fractured rock, *Water Resour. Res.*, *24*(10), 1796–1804, doi:10.1029/WR024i010p01796.

Bear, J., et al. (1993), *Flow and Contaminant Transport in Fractured Rock*, Academic, San Diego, Calif.

Bonnet, E., et al. (2001), Scaling of fracture systems in geological media, *Rev. Geophys.*, *39*(3), 347–383, doi:10.1029/1999RG000074.

Bouchaud, E., et al. (1990), Fractal dimension of fractured surfaces: A universal value?, *Europhys. Lett.*, *13*, 73–79, doi:10.1209/0295-5075/13/1/013.

Bour, O., and P. Davy (1998), On the connectivity of three dimensional fault networks, *Water Resour. Res.*, *34*(10), 2611–2622, doi:10.1029/98WR01861.

Bour, O., and P. Davy (1999), Clustering and size distributions of fault patterns: Theory and measurements, *Geophys. Res. Lett.*, *26*(13), 2001–2004, doi:10.1029/1999GL900419.

Brezzi, F., and M. Fortin (1991), *Mixed and Hybrid Finite Element Methods*, Springer, Berlin, doi:10.1007/978-1-4612-3172-1.

Brown, S. (1987), Fluid flow through rock joints: The effect of surface roughness, *J. Geophys. Res.*, *92*(B2), 1337–1347, doi:10.1029/JB092iB02p01337.

Brown, S. R. (1995), Simple mathematical model of rough fracture, *J. Geophys. Res.*, *100*(B4), 5941–5952, doi:10.1029/94JB03262.

Brown, S. R., and C. H. Scholz (1985), Broad bandwidth study of the topography of natural rock surfaces, *J. Geophys. Res.*, *90*, 12,575–12,582, doi:10.1029/JB090iB14p12575.

Brown, S. R., et al. (1986), Correlation between the surfaces of natural rock joints, *Geophys. Res. Lett.*, *13*(13), 1430–1433, doi:10.1029/GL013i013p01430.

Brown, S. R., et al. (1995), Applicability of the Reynolds equation for modeling fluid flow between rough surfaces, *Geophys. Res. Lett.*, *22*(18), 2537–2540, doi:10.1029/95GL02666.

Cacas, M. C., et al. (1990a), Modeling fracture flow with a stochastic discrete fracture network: Calibration and validation: 1. The flow model, *Water Resour. Res.*, *26*(3), 479–489.

Cacas, M. C., et al. (1990b), Modeling fracture flow with a stochastic discrete fracture network: Calibration and validation: 2. The transport model, *Water Resour. Res.*, *26*(3), 491–500.

Cappa, F., et al. (2006), Hydromechanical modelling of pulse tests that measure fluid pressure and fracture normal displacement at the Coaraze Laboratory site, France, *Int. J. Rock Mech. Min. Sci.*, *43*(7), 1062–1082, doi:10.1016/j.ijrmms.2006.03.006.

Cello, P. A., et al. (2009), Flow dimension and anomalous diffusion of aquifer tests in fracture networks, *Vadose Zone J.*, *8*(1), 258–268, doi:10.2136/vzj2008.0040.

Charlaix, E., et al. (1987), Permeability of a random array of fractures of widely varying apertures, *Transp. Porous Media*, *2*, 31–43, doi:10.1007/BF00208535.

Clauser, C. (1992), Permeability of crystalline rock, *Eos Trans. AGU*, *73*(21), 233, doi:10.1029/91EO00190.

Cook, N. G. W. (1992), Natural joints in rock: Mechanical, hydraulic and seismic behavior and properties under normal stress, *Int. J. Mech. Min. Sci. Geomech. Abstr.*, *29*(3), 198–223, doi:10.1016/0148-9062(92)93656-5.

Darcel, C., et al. (2003a), Cross-correlation between length and position in real fracture networks, *Geophys. Res. Lett.*, *30*(12), 1650, doi:10.1029/2003GL017174.

Darcel, C., et al. (2003b), Stereological analysis of fractal fracture networks, *J. Geophys. Res.*, *108*(B9), 2451, doi:10.1029/2002JB002091.

Davis, T. A., and I. S. Duff (1999), A combined unifrontal multifrontal method for unsymmetric sparse matrices, *Trans. Math. Software*, *25*(1), 1–20, doi:10.1145/305658.287640.

Davy, P., et al. (2006a), Flow in multiscale fractal fracture networks, *Geol. Soc. Spec. Publ.*, *261*, 31–45.

Davy, P., et al. (2006b), A note on the angular correction applied to fracture intensity profiles along drill core, *J. Geophys. Res.*, *111*, B11408, doi:10.1029/2005JB004121.

Davy, P., et al. (2010), A likely universal model of fracture scaling and its consequence for crustal hydromechanics, *J. Geophys. Res.*, *115*, B10411, doi:10.1029/2009JB007043.

de Dreuzy, J.-R., and P. Davy (2007), Relation between fractional flow models and fractal or long-range 2-D permeability fields, *Water Resour. Res.*, *43*, W04431, doi:10.1029/2006WR005236.

de Dreuzy, J. R., et al. (2000), Percolation threshold of 3D random ellipses with widely scattered distributions of eccentricity and size, *Phys. Rev. E*, *62*(5), 5948–5952, doi:10.1103/PhysRevE.62.5948.

de Dreuzy, J. R., et al. (2001a), Advective transport in the percolation backbone in two dimensions, *Phys. Rev. E*, *64*, 056305.

de Dreuzy, J. R., et al. (2001b), Hydraulic properties of two-dimensional random fracture networks following a power law length distribution: 2. Permeability of networks based on log-normal distribution of apertures, *Water Resour. Res.*, *37*(8), 2079–2095, doi:10.1029/2001WR900010.

de Dreuzy, J. R., et al. (2001c), Hydraulic properties of two-dimensional random fracture networks following a power law length distribution: 1. Effective connectivity, *Water Resour. Res.*, *37*(8), 2065–2078.

de Dreuzy, J. R., et al. (2002), Permeability of 2D fracture networks with power-law distributions of length and aperture, *Water Resour. Res.*, *38*(12), 1276, doi:10.1029/2001WR001009.

de Dreuzy, J.-R., et al. (2004a), Influence of spatial correlation of fracture centers on the permeability of two-dimensional fracture networks following a power law length distribution, *Water Resour. Res.*, *40*, W01502, doi:10.1029/2003WR002260.

de Dreuzy, J. R., et al. (2004b), Anomalous diffusion exponents in continuous two-dimensional multifractal media, *Phys. Rev. E*, *70*(1), 016306, doi:10.1103/PhysRevE.70.016306.

de Dreuzy, J.-R., et al. (2010), Use of power-averaging for quantifying the influence of structure organization on permeability upscaling, *Water Resour. Res.*, *46*, W08519, doi:10.1029/2009WR008769.

de Dreuzy, J.-R., et al. (2012), Synthetic benchmark for modeling flow in 3D fractured media, *Comput. Geosci.*, doi:10.1016/j.cageo.2012.07.025, in press.

Dershowitz, W. S., and C. Fidelibus (1999), Derivation of equivalent pipe networks analogues for three-dimensional discrete fracture networks by the boundary element method, *Water Resour. Res.*, *35*(9), 2685–2691, doi:10.1029/1999WR900118.

Desbarats, A. J. (1992), Spatial averaging of transmissivity in heterogeneous fields with flow toward a well, *Water Resour. Res.*, *28*(3), 757–767, doi:10.1029/91WR03099.

Detwiler, R. L., et al. (1999), Measurement of fracture aperture fields using transmitted light: An evaluation of measurement errors and their influence on simulations of flow and transport through a single fracture, *Water Resour. Res.*, *35*(9), 2605–2617, doi:10.1029/1999WR900164.

Durham, W. B. (1997), Laboratory observations of the hydraulic behavior of a permeable fracture from 3800 m depth in the KTB pilot hole, *J. Geophys. Res.*, *102*(B8), 18,405–18,416, doi:10.1029/96JB02813.

Durham, W. B., and B. P. Bonner (1995), Closure and fluid flow in discrete fractures, in *Fractured and Jointed Rock Masses*, edited by L. R. Myer et al., pp. 441–446, A. A. Balkema, Rotterdam, Netherlands.

Erhel, J., et al. (2009a), Flow simulation in three-dimensional discrete fracture networks, *SIAM J. Sci. Comput.*, *31*(4), 2688–2705, doi:10.1137/080729244.

Erhel, J., et al. (2009b), A parallel scientific software for heterogeneous hydrogeology, in *Parallel Computational Fluid Dynamics 2007*, *Lect. Notes in Comput. Sci. and Eng.*, vol. 67, pp. 39–48, Springer, Berlin.

Erhel, J., et al. (2011), Multi-parametric intensive stochastic simulations for hydrogeology on a computational grid, in *Parallel Computational Fluid Dynamics*, *Lect. Notes in Comput. Sci. and Eng.*, vol. 74, pp. 389–397, Springer, Berlin.

Frampton, A., and V. Cvetkovic (2007), Upscaling particle transport in discrete fracture networks: 1. Nonreactive tracers, *Water Resour. Res.*, *43*, W10428, doi:10.1029/2006WR005334.

Frampton, A., and V. Cvetkovic (2009), Significance of injection modes and heterogeneity on spatial and temporal dispersion of advecting particles in two-dimensional discrete fracture networks, *Adv. Water Resour.*, *32*(5), 649–658, doi:10.1016/j.advwatres.2008.07.010.

Glover, P. W. J., et al. (1998), Synthetic rough fractures in rocks, *J. Geophys. Res.*, *103*(B5), 9609–9620, doi:10.1029/97JB02836.

Hamzehpour, H., et al. (2009), Percolation and permeability of networks of heterogeneous fractures, *Phys. Rev. E*, *79*(3), 036302.

Hoshen, J. (1997), Percolation and cluster structure parameters: The enhanced Hoshen-Kopelman algorithm, *Phys. Rev. E*, *56*(2), 1455–1460, doi:10.1103/PhysRevE.56.1455.

Hsieh, P. A. (1998), Scale effects in fluid flow through fractured geological media, in *Scale Dependence and Scale Invariance in Hydrology*, pp. 335–353, Cambridge Univ. Press, Cambridge, U. K., doi:10.1017/CBO9780511551864.013.

Hsieh, P. A., et al. (1993), Methods of characterizing fluid movement and chemical transport in fractured rock, in *Field Trip Guidebook for Northeastern United States*, edited by J. T. Cheney and J. C. Hepburn, pp. R1–R30, Geol. Soc. of Am., Boulder, Colo.

Hunt, A. G., and G. W. Gee (2002), Application of critical path analysis to fractal porous media: Comparison with examples from the Hanford site, *Adv. Water Resour.*, *25*(2), 129–146, doi:10.1016/S0309-1708(01)00057-4.

Isakov, E., et al. (2001), Fluid flow through rough fractures in rocks I: High resolution aperture determinations, *Earth Planet. Sci. Lett.*, *191*(3–4), 267–282, doi:10.1016/S0012-821X(01)00424-1.

Ji, S. H., et al. (2011), Influence of fracture connectivity and characterization level on the uncertainty of the equivalent permeability in statistically conceptualized fracture networks, *Transp. Porous Media*, *87*(2), 385–395, doi:10.1007/s11242-010-9690-9.

Johnson, K. L. (1985), *Contact Mechanics*, Cambridge Univ. Press, Cambridge, U. K.

Jourde, H., et al. (2007), Relationship between the geometrical and structural properties of layered fractured rocks and their effective permeability tensor. A simulation study, *J. Hydrol.*, *337*(1–2), 117–132, doi:10.1016/j.jhydrol.2007.01.027.

Kalbacher, T., et al. (2007), Geometric modelling and object-oriented software concepts applied to a heterogeneous fractured network from the Grimsel rock laboratory, *Computat. Geosci.*, *11*(1), 9–26, doi:10.1007/s10596-006-9032-8.

Le Borgne, T., et al. (2004), Equivalent mean flow models for fractured aquifers: Insights from a pumping tests scaling interpretation, *Water Resour. Res.*, *40*, W03512, doi:10.1029/2003WR002436.

L'Ecuyer, P., et al. (2002), An object-oriented random-number package with many long streams and substreams, *Oper. Res.*, *50*(6), 1073–1075, doi:10.1287/opre.50.6.1073.358.

Le Goc, R., et al. (2010), Statistical characteristics of flow as indicators of channeling in heterogeneous porous and fractured media, *Adv. Water Resour.*, *33*(3), 257–269, doi:10.1016/j.advwatres.2009.12.002.

Lenti, V., and C. Fidelibus (2003), A BEM solution of steady-state flow problems in discrete fracture networks with minimization of core storage, *Comput. Geosci.*, *29*(9), 1183–1190, doi:10.1016/S0098-3004(03)00140-7.

Leung, C. T. O., and R. W. Zimmerman (2010), Estimating the hydraulic conductivity of two-dimensional fracture networks using effective medium theory and power-law averaging, in *Rock Mechanics in Civil and Environmental Engineering*, pp. 243–246, CRC Press, Boca Raton, Fla.

Long, J. C. S., and P. A. Witherspoon (1985), The relationship of the degree of interconnection to permeability in fracture networks, *J. Geophys. Res.*, *90*(B4), 3087–3098, doi:10.1029/JB090iB04p03087.

Long, J. C. S., et al. (1982), Porous media equivalents for networks of discontinuous fractures, *Water Resour. Res.*, *18*(3), 645–658, doi:10.1029/WR018i003p00645.

Long, J. C. S., et al. (1985), A model for steady fluid flow in random three-dimensional networks of disc-shaped fractures, *Water Resour. Res.*, *21*(8), 1105–1115, doi:10.1029/WR021i008p01105.

Maryka, J., et al. (2004), Numerical simulation of fracture flow with a mixed-hybrid FEM stochastic discrete fracture network model, *Comput. Geosci.*, *8*(3), 217–234.

Matheron, G. (1967), *Eléments Pour une Théorie des milieux Poreux*, Masson, Paris.

Méheust, Y., and J. Schmittbuhl (2000), Flow enhancement of a rough fracture, *Geophys. Res. Lett.*, *27*(18), 2989–2992, doi:10.1029/1999GL008464.

Méheust, Y., and J. Schmittbuhl (2001), Geometrical heterogeneities and permeability anisotropy of rough fractures, *J. Geophys. Res.*, *106*(B2), 2089–2102, doi:10.1029/2000JB900306.

Méheust, Y., and J. Schmittbuhl (2003), Scale effects related to flow in rough fractures, *Pure Appl. Geophys.*, *160*(5–6), 1023–1050, doi:10.1007/PL00012559.

Mettier, R., et al. (2006), Influence of small-scale heterogeneities on contaminant transport in fractured crystalline rock, *Ground Water*, *44*(5), 687–696, doi:10.1111/j.1745-6584.2006.00236.x.

Mustapha, H. (2005), Simulation numérique de l'écoulement dans des milieux fracturés tridimensionnels, PhD thesis, Univ. of Rennes 1, Rennes, France.

National Research Council (1996), *Rock Fractures and Fluid Flow*, Natl. Acad. Press, Washington, D. C.

Neuman, S. P. (2005), Trends, prospects and challenges in quantifying flow and transport through fractured rocks, *Hydrogeol. J.*, *13*(1), 124–147, doi:10.1007/s10040-004-0397-2.

Noetinger, B., and N. Jarrige (2012), A quasi steady state method for solving transient Darcy flow in complex 3D fractured networks, *J. Comput. Phys.*, *231*(1), 23–38, doi:10.1016/j.jcp.2011.08.015.

Nordqvist, A. W., et al. (1996), Effects of high variance of fracture transmissivity on transport and sorption at different scales in a discrete model for fractured rocks, *J. Contam. Hydrol.*, *22*(1–2), 39–66, doi:10.1016/0169-7722(95)00064-X.

Painter, S., and V. Cvetkovic (2005 Upscaling discrete fracture network simulations: An alternative to continuum transport models, *Water Resour. Res.*, *41*, W02002, doi:10.1029/2004WR003682.

Park, Y.-J., et al. (2001), Transport and intersection mixing in random fracture networks with power law length distributions, *Water Resour. Res.*, *37*(10), 2493–2501, doi:10.1029/2000WR000131.

Persson, B. N. J. (2001), Elastoplastic contact between randomly rough surfaces, *Phys. Rev. Lett.*, *87*(11), 116101, doi:10.1103/PhysRevLett.87.116101.

Persson, B. N. J., F. Bucher, and B. Chiaia (2002), Elastic contact between randomly rough surfaces: Comparison of theory with numerical results, *Phys. Rev. B*, *65*(18), 184106, doi:10.1103/PhysRevB.65.184106.

Pichot, G., et al. (2010), A mixed hybrid mortar method for solving flow in discrete fracture networks, *Appl. Anal.*, *89*(10), 1629–1643, doi:10.1080/00036811.2010.495333.

Pichot, G., et al. (2012), Flow simulation in 3D multi-scale fractured networks using non-matching meshes, *SIAM J. Sci. Comput.*, *34*(1), B86–B105.

Piggot, A. R. (1997), Fractal relations for the diameter and trace length of disc-shaped fractures, *J. Geophys. Res.*, *102*(B8), 18,121–18,125.

Poirriez, B. (2011), Étude et mise en oeuvre d'une méthode de sous-domaines pour la modélisation de l'écoulement dans des réseaux de fractures en 3D, PhD thesis, Univ. of Rennes 1, Rennes, France.

Power, W. L., and W. B. Durham (1997), Topography of natural and artificial fractures in granitic rocks: Implications for studies of rock friction and fluid migration, *Int. J. Rock Mech. Min. Sci.*, *34*(6), 979–989, doi:10.1016/S1365-1609(97)80007-X.

Pyrak-Nolte, L. J., and J. P. Morris (2000), Single fractures under normal stress: The relation between fracture specific stiffness and fluid flow, *Int. J. Rock Mech. Min. Sci.*, *37*(1–2), 245–262.

Raviart, P. A., and J. M. Thomas (1977), A mixed finite element method for second order elliptic problems, in *Mathematical Aspects of the Finite Element Method*, *Lect. Notes in Math.*, vol. 606, pp. 292–315, Springer, New York, doi:10.1007/BFb0064470.

Renard, P., and G. de Marsily (1997), Calculating equivalent permeability: A review, *Adv. Water Resour.*, *20*(5–6), 253–278, doi:10.1016/S0309-1708(96)00050-4.

Ronayne, M. J., and S. M. Gorelick (2006), Effective permeability of porous media containing branching channel networks, *Phys. Rev. E*, *73*(2), 026305, doi:10.1103/PhysRevE.73.026305.

Rubin, Y., and S. Hubbard (2006), *Hydrogeophysics*, Springer, Dordrecht, Netherlands.

Sahimi, M. (1993), Flow phenomena in rocks: From continuum models to fractals, percolation, cellular automata, and simulated annealing, *Rev. Mod. Phys.*, *65*(4), 1393–1534, doi:10.1103/RevModPhys.65.1393.

Schmittbuhl, J., et al. (1993), Field-measurements of the roughness of fault surfaces, *Geophys. Res. Lett.*, *20*(8), 639–641, doi:10.1029/93GL00170.

Schmittbuhl, J., et al. (1995), Scaling invariance of crack surfaces, *J. Geophys. Res.*, *100*(B4), 5953–5973, doi:10.1029/94JB02885.

Segall, P., and D. D. Pollard (1983), Joint formation in granitic rock of the Sierra-Nevada, *Geol. Soc. Am. Bull.*, *94*(5), 563–575, doi:10.1130/0016-7606(1983)94<563:JFIGRO>2.0.CO;2.

Snow, D. T. (1969), Anisotropic permeability of fractured media, *Water Resour. Res.*, *6*, 1273–1289, doi:10.1029/WR005i006p01273.

Stauffer, D., and A. Aharony (1992), *Introduction to Percolation Theory*, 2nd ed., Taylor and Francis, Bristol, U. K.

Talon, L., et al. (2010a), Permeability estimates of self-affine fracture faults based on generalization of the bottleneck concept, *Water Resour. Res.*, *46*, W07601, doi:10.1029/2009WR008404.

Talon, L., et al. (2010b), Permeability of self-affine aperture fields, *Phys. Rev. E*, *82*(4), 046108, doi:10.1103/PhysRevE.82.046108.

Thompson, M. E. (1991), Numerical simulation of solute transport in rough fractures, *J. Geophys. Res.*, *96*(B3), 4157–4166, doi:10.1029/90JB02385.

Thompson, M., and S. Brown (1991), The effect of anisotropic surface-roughness on flow and transport in fractures, *J. Geophys. Res.*, *96*(B13), 21,923–21,932, doi:10.1029/91JB02252.

Tsang, C.-F., and I. Neretnieks (1998), Flow channeling in heterogeneous fractured rocks, *Rev. Geophys.*, *36*(2), 275–298, doi:10.1029/97RG03319.

Vohralik, M., et al. (2007), Mixed and nonconforming finite element methods on a system of polygons, *Appl. Numer. Math.*, *57*(2), 176–193, doi:10.1016/j.apnum.2006.02.005.

Wellman, T. P., et al. (2009), Effects of simplifying fracture network representation on inert chemical migration in fracture-controlled aquifers, *Water Resour. Res.*, *45*, W01416, doi:10.1029/2008WR007025.

Witherspoon, P., et al. (1979), Observations of a potential size effect in experimental determination of the hydraulic properties of fractures, *Water Resour. Res.*, *15*(5), 1142–1146, doi:10.1029/WR015i005p01142.

Witherspoon, P. A., et al. (1980), Validity of cubic law for fluid-flow in a deformable rock fracture, *Water Resour. Res.*, *16*(6), 1016–1024, doi:10.1029/WR016i006p01016.

Yeh, T. C. J., and S. Y. Liu (2000), Hydraulic tomography: Development of a new aquifer test method, *Water Resour. Res.*, *36*(8), 2095–2105, doi:10.1029/2000WR900114.

Zimmerman, R. W., and G. S. Bodvarsson (1996a), Hydraulic conductivity of rock fractures, *Transp. Porous Media*, *23*(1), 1–30, doi:10.1007/BF00145263.

Zimmerman, R. W., and G. S. Bodvarsson (1996b), Hydraulic conductivity of rock fractures, *Transp. Porous Media*, *23*, 1–30.

Zimmerman, R. W., and G. S. Bodvarsson (1996c), Effective transmissivity of two-dimensional fracture networks, *Int. J. Mech. Min. Sci. Geomech. Abstr.*, *33*(4), 433–438, doi:10.1016/0148-9062(95)00067-4.